Unified modelling of adiabatic shear banding and subsequent micro-voiding driven dynamic failure of viscoplastic solids

Hannah Lois Dorothy, Patrice Longère

Unified modelling of adiabatic shear banding and subsequent micro-voiding driven dynamic failure of viscoplastic solids

Hannah Lois Dorothy[a], Patrice Longère[a]

[a]*Université de Toulouse, UT3-UPS, ISAE-SUPAERO, Institut Clément Ader (CNRS 5312), 3 rue Caroline Aigle, 31400 TOULOUSE, France*

ABSTRACT

Adiabatic shear bands (ASBs) are intense shear localisation zones resulting from thermomechanical instability in dynamically loaded, high strength structural materials. In the wake of the ASB, Micro-voids (MVs) have been observed which coalesce and ultimately rupture the material. ASBs thus favour premature MV induced damage and further material failure. In the present work, the coupled effects of ASB+MV on the representative volume element (RVE) are reproduced in a unified model within irreversible thermodynamics framework considering a large scale postulate. The influence of the softening mechanisms such as thermal softening and/or DRX induced softening on the ASB onset is accounted for. The model is numerically implemented as a user material subroutine into the engineering finite element (FE) computation code LS-DYNA and its feasibility and performances are assessed on both RVE and structural scales. The dynamic shear compression loading of a hat shaped structure is simulated for that purpose. The respective contributions of ASB and MV on the progressive material deterioration can be clearly identified.

Keywords:

Adiabatic shear banding, Ductile damage, Dynamic plasticity, Numerical simulation

1 INTRODUCTION

The present study aims at modelling the adiabatic shear banding and the consecutive micro-voiding induced material deterioration. Adiabatic shear banding is a distinct deformation mechanism which occurs in viscoplastic solids during high strain rate and impact loading acting as a precursor to failure such as plugging failure, ductile fracture, explosive failure, etc., see [1],[2],[3]. The Adiabatic Shear Bands (ASBs) are seen typically in high strength metals and alloys such as steels and titanium and aluminium alloys which are often used as component materials for aircraft and other structures. The ASBs are undesirable when they cause catastrophic failures of structures such as

protection plates for ballistic applications [4] involving military or civil threats (missile, bird strike, etc). On the other hand, they are desirable in military application such as kinetic energy penetrators in which the formation of ASBs on the side ends of the penetrator helps in a self-sharpening-like mechanism ([5],[6],[7]). They also find industrial application in high speed machining in which they have mitigated effect in the sense that they help to reduce the cutting force but at the expense of cutting force oscillation and rougher surface finish [8],[9]. In the context of engineering design, it is thus crucial to be able to numerically reproduce the consequences of this phenomenon.

The ASBs are narrow regions of intense plastic shear deformation and strength softening resulting from thermo-mechanical instability induced by a competition between hardening and softening mechanisms in the regions of low stress triaxiality during high strain rate loading. The mechanisms causing the softening which triggers the ASB formation are mostly plastic dissipation-induced temperature rise and possibly dynamic recrystallization (DRX) in certain materials. The shear bands are distinctly oriented causing local degradation of the material properties and a form of induced anisotropy at the scale of the specimen. Once the ASB is formed, the softer material within the band serves as a site for the nucleation and growth of micro-voids (MV). These micro-voids additionally contribute to softening mechanism and accelerate the post-localization drop in strength of the RVE in the large scale postulate framework. The micro-voids coalesce and lead to the formation of cracks which ultimately fracture the material. The evidence of the presence of micro-voids within the ASB was shown by various experimental observations ([10],[2],[11]). The experimental observation reported in on the fracture surface of impacted shear compression specimens showed the evidence of micro-voids in the ASB wake which proved that the fracture occurred due to two successive mechanisms: adiabatic shear banding and then micro-voiding.

The ASB in itself is a weak discontinuity, causing shape change, as there is cohesion of matter within the band; the MV is a strong discontinuity with the absence of matter within, creating irreversible damage in the material and imposing volume change and related hydrostatic components to the induced strain rate because of the void growth. Depending on the loading, the ASB does not necessarily lead to micro-voiding and further failure; and in certain cases, upon unloading, the ASB is quenched by the cooler surrounding material, undergoes phase transformation and finally becomes harder at room temperature than the surrounding matrix material [12]. Therefore considering a unique variable accounting indistinctly for ASB and MV does not allow for distinguishing the zones in the structure where ASB takes place, with potential initial properties recovering after unloading and cooling as explained above, and where irreversible void-growth induced irreversible damage as a precursor to crack formation takes place. Being able to distinguish the respective contributions of ASB and MV on the current (during

loading) and residual (post loading) material deterioration is accordingly of major interest.

Many approaches describing the ASB in the literature are developed at a scale lower than the bandwidth ([13], [14]and [15]). However, as the ASB width in itself is of the order of micro-meters, this postulate requires the use of very fine meshing in the finite element (FE) simulations. Whereas in the present study, a large scale postulate is adopted, in which the representative volume element (RVE) has a length scale greater than the ASB width; in other words, the shear band is embedded within the RVE. This approach facilitates the use of coarser meshes in FE simulations and thus makes the model feasible to implement on engineering structural applications. Large scale approaches based on variational methods and enriched finite elements can be found in [16], [17], [18] and [19], and a review of ASB-oriented modelling approaches in [20]. While modelling of ASB can be widely found in the literature, the subsequent mechanism of micro-voiding and its modelling as a distinct contribution to the failure process is largely overlooked. The present work aims to model in a unified approach the ASB and subsequent MV induced degradation.

A physics motivated phenomenological three-dimensional constitutive model was initially developed by Longère et al. [21] in an irreversible thermodynamics framework which described the material degradation induced predominantly by the ASB. The aim here is to use an enlarged version of the aforementioned model based on the model developed recently by Longère and Dragon [22] in order to explicitly reproduce the consequences of micro-voiding in the band wake. The view is to clearly distinguish in the post-critical regime the respective contributions to the material softening coming from the two mechanisms at stake, namely adiabatic shear banding on one hand and micro-voiding on the other hand. The ASB+MV model is here implemented as user material into the engineering finite element (FE) computation code LS-DYNA in the context of standard FE kinematic formulation. The numerical feasibility of the enriched model and the results showing the distinct ASB and MV effects are then demonstrated on the RVE and structural scales.

Section 2 presents the development of the constitutive model. The numerical issues encountered in the finite element implementation and performance of enriched ASB+MV model is assessed by numerical implementation on RVE scale and initial boundary value problems (IBVP) in Section 3. Finally the conclusions are drawn in Section 4 and some prospective work is suggested.

2 BASIC CONCEPTS AND CONSTITUTIVE MODELLING

The physical aspects and mechanical consequences of ASB and MV are presented below followed by the development of the constitutive model in an irreversible thermodynamics framework.

2.1 PHYSICAL AND MECHANICAL ASPECTS

The high strength metals and alloys under high strain rate loading first exhibit elasto-plasticity. During this stage, the self-heating caused by plastic dissipation and/or softening due to dynamic recrystallization may lead to the formation of a localized shear deformation (ASB) which causes material strength deterioration and alters the kinematics of the plastic flow. Further, damage is encountered within the shear bands causing the material failure. The scenario for ASB and MV assisted failure which is considered for modelling in the present study and their effects on the shear stress-shear strain curve are depicted in Fig. 1. The regular mechanism of polycrystalline plasticity is in action during the initial stage of hardening. Then the formation of the ASB reduces the material strength. The drop in the material strength in the post critical stage is potentially accelerated by the formation of micro-voids in the wake of the ASB. The micro-voids coalesce and ultimately rupture the material.

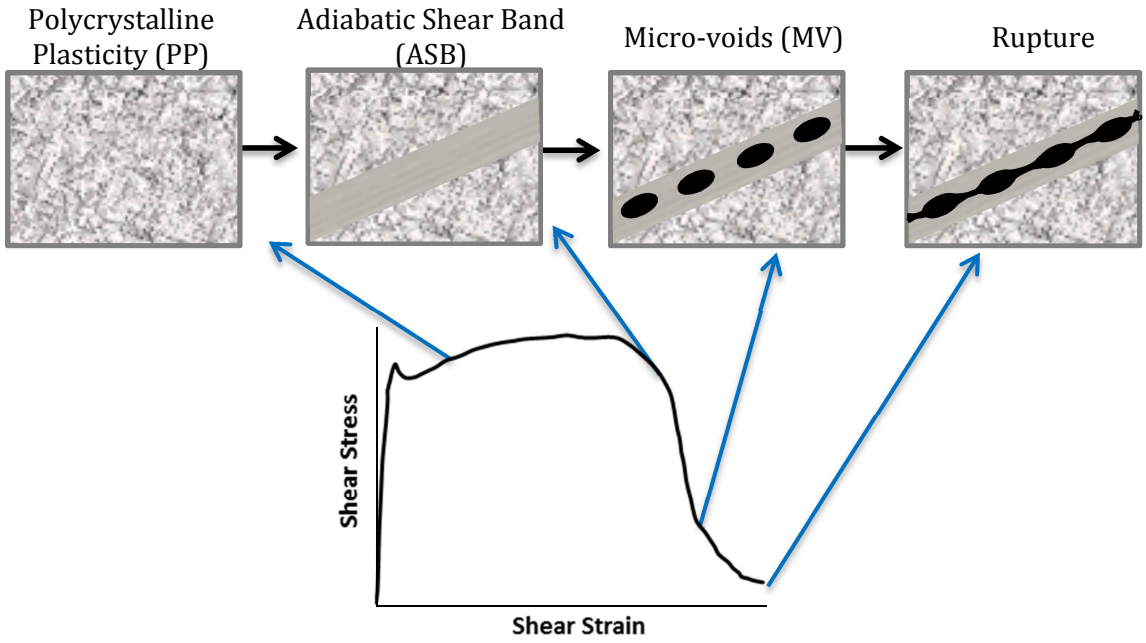

Fig. 1 Successive mechanisms acting during ASB induced deterioration. Schematic drawings of microstructures are inspired from [2], see Fig.8 therein, and of shear stress-shear strain curve from [23], see Fig.12 therein.

In the following subsections, the salient physical and mechanical features involved are presented.

2.1.1 Physical considerations

The physical features and the formation process of the adiabatic shear bands and micro-voids are presented in this section.

2.1.1.1 Adiabatic shear banding

As mentioned above, the ASBs are distinctly oriented shear localizations resulting from a thermo-mechanical instability phenomenon. The heat produced from the plastic deformation during high strain rate loading, when not having enough time to be conducted away leads to local increase in temperature giving rise to a 'quasi-adiabatic' condition. This causes a local thermal softening of the material. Thermo-mechanical instability comes into play as a competition arises between the thermal softening and strain or/and strain-rate hardening. When the rate of this thermal softening surpasses the strain/strain rate hardening, the material deformation becomes unstable and concentrates in narrow softened bands which are termed as ASBs. This widely accepted mechanism of ASB inception and growth was first proposed by Zener and Hollomon [24]. For certain alloys such as those of titanium, DRX is shown to contribute significantly to the softening leading to the formation of ASB (see [25],[26])

2.1.1.2 Micro-voiding in the ASB wake

Although the ASBs occur in conditions of negative or nil stress triaxiality, micro-voids have been observed to form and grow within the bands. The micro-voiding could be initiated in the band wake by the hydrostatic tension when there is a change in the loading path. Or as stated in [20], when the loading is interrupted after the formation of the ASB, the quenching of the hot band by the surrounding bulk material may lead to phase transformation involving possible volume increase (as for martensitic transformation) and strain incompatibility-induced crack formation at the band/matrix interface. However, the ASB induced failure is generally observed under monotonic loading.

Various perspectives on the stress triaxiality condition for the formation of micro-voids have been proposed which is discussed in section 3.1.1.3. Under a global shear pressure loading, Longère et al. [27] demonstrated that micro-voids can initiate and grow around inclusions in the material. Another theory cited by Odeshi et al. [11] is that the opening of the voids could be because of the high singular temperatures within the ASB causing

atomic mobility or creating a lower flow stress in the ASB than the surrounding regular material thereby generating a local tensile stress.

2.1.1.3 Ultimate rupture

The ASB by itself is not a failure mode i.e. a strong discontinuity but it acts as a precursor to premature material failure. The micro-voids which germinate within the ASB coalesce to the formation of cracks leading to the ultimate rupture of the material. Liu et al. [28] performed dynamic compression on Ti6Al4V alloy cylinders leading to ASB induced failure. The microscopic observation of the crushed specimens showed ASBs containing voids and coalesced voids (cracks).

2.1.2 Mechanical consequences

The mechanical consequences of ASB+MV initiation and evolution on the RVE (material point) response are double: material and kinematic.

2.1.2.1 Preliminaries

ASBs are not a type of crack or a conventional 'damage' as there is cohesion of matter within the bands and without any surface separation. Neither are they slip bands which occur under quasi static conditions as the physics of the phenomenon is different. What is observed is a large gradient of the shear strain between the matrix and the band. It is considered here as a 'degradation' mechanism as it degrades the mechanical properties of the overall material/structure in which it is present.

ASBs are therefore classified as 'weak' discontinuity which involves a discontinuity of the gradient of the displacement/velocity i.e. of the strain/strain rate field. A 'strong' discontinuity such as a crack on the other hand involves a discontinuity of the displacement/velocity field. The weak discontinuity (ASB) serves as the path for the initiation of micro-voids which coalesce to form a strong discontinuity (crack) and the material fails. Like the ASB, the micro-voids formed in the wake of the ASB also have an effect on the deterioration and kinematic response of the material.

In the present study, a large scale postulate is adopted, in which the representative volume element (RVE) has a length scale W greater than the ASB width λ, i.e. $W > \lambda$; in other words, the shear band is embedded within the RVE. In the presence of ASB coexist two different deformation patterns inside the medium: a 'regular' one relative to the material outside the bands, and a 'singular' one relative to the material inside the bands, see [21], [29]. Let suppose that the evolution of 'regular' and 'singular' processes can be

described via the evolution of state variables such like relevant measures of elastic strain $\mathbf{e}^{\mathbf{e}}$, temperature T, strain hardening κ, damage δ, metallurgical state ξ, and so on :

$$V_{\text{regular}} = \left(\mathbf{e}^{\mathbf{e}}, T, \kappa, \delta, \xi, \ldots\right) \text{ and } V_{\text{singular}} = \left(\mathbf{e}^{\mathbf{e}}*, T*, \kappa*, \delta*, \xi*, \ldots\right)$$

where V_{regular} and V_{singular} represent respectively the sets of 'regular' and 'singular' state variables. At an advanced stage of deformation, 'singular' elastic strain can be neglected, while a specific 'singular' variable describing intense shearing will be introduced further. We then have tentatively:

$$V_{\text{regular}} = \left(\mathbf{e}^{\mathbf{e}}, T, \kappa, \delta, \xi, \ldots\right) \text{ and } V_{\text{singular}} = \left(T*, \kappa*, \delta*, \xi*, \ldots\right)$$

Before the ASB onset, solely 'regular' processes run:

$$V_{\text{regular}} = \left(\mathbf{e}^{\mathbf{e}}, T, \kappa, \delta, \xi, \ldots\right) \text{ and } V_{\text{singular}} = \left(0, 0, 0, 0, \ldots\right)$$

After the ASB onset, evolutions of 'regular' and 'singular' processes, associated to RVE whose length scale W is greater than the band width λ, i.e. $W > \lambda$, and which are respectively located outside and inside the band, become significantly distinct:

$$V_{\text{regular}} = \left(\mathbf{e}^{\mathbf{e}}, T, \kappa, \delta, \xi, \ldots\right) \text{ and } V_{\text{singular}} = \left(T*, \kappa*, \delta*, \xi*, \ldots\right)$$

In our approach, the evolution of the 'singular' dissipative processes (intervening inside the band) contributing to this macromechanical softening is described via the evolution of a single internal variable called $\mathcal{D}$. The softening of the RVE behaviour being considered as a form of mechanical degradation, the variable $\mathcal{D}$ must then be able to describe the deterioration state of the RVE induced by the presence of the bands (ASB related feedback deterioration).

The variable $\mathcal{D}$ is then a function of the 'singular' state variables and of the characteristic length λ of the band:

$$\mathcal{D} = \mathcal{D}\left(V_{\text{singular}}\right) = \mathcal{D}\left(\lambda, T*, \kappa*, \delta*, \xi*, \ldots\right)$$

A micromechanical analysis followed by any averaging procedure could have lead to an explicit form for $\mathcal{D}$. This is not the purpose of the present work as it is hardly feasible regarding strongly non-linear phenomena involved and high strain rate context. What we are putting forward is a phenomenological description involving 'singular'

dissipative evolution due to ASB and further micro-voiding entirely incorporated in the evolution of $\mathcal{D}$. In our phenomenological approach, evolution law of $\mathcal{D}$ is derived from the normality rule under the assumption of the existence of a corresponding dissipative potential.

2.1.2.2 Orientation

According to the large scale postulate, the shear band or the shear band cluster is considered as an entity embedded within the RVE, see Fig. 2. The vector $\mathbf{g}$ is collinear to the slip direction in the band plane and $\mathbf{n}$ represents the normal to the band plane. Accordingly, the structural tensors used in the following are defined in (1) where $()^S$ represents the symmetric and $()^{AS}$ the skew-symmetric parts of the tensor. According to experimental evidences, the ASBs develop along the planes of maximum shear stress within the RVE and thus their orientations are calculated.

$$\mathbf{N} = \mathbf{n}\otimes\mathbf{n}\ ;\ \mathbf{M} = (\mathbf{g}\otimes\mathbf{n})^{S}\ ;\ \mathbf{T} = (\mathbf{g}\otimes\mathbf{n})^{AS} \tag{1}$$

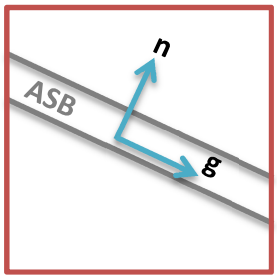

Fig. 2 ASB embedded within the RVE and orientation vectors

Different configurations of micro-voids developing in the ASB wake can be distinguished. A thick wall cylinder implosion technique was carried out by Xue et al. [2] to produce shear bands on Ti-6Al-4V alloys. The microscopic observation of the ASB showed spherical void nucleation. The spherical voids were later seen to elongate to ellipse shape rotate along the direction of the maximum shear stress. Impact tests on hat shaped specimen by Peirs. et al. [1] showed micro-cracks in the wake of the ASB oriented along the highly deformed grains which is different from the ASB orientation. Accordingly, Fig. 3 shows an illustration of the possible micro-void shape and orientation vectors $\mathbf{n}^*, \mathbf{g}^*$ for micro-voiding occurring inside the band. Corresponding MV structural tensors are denoted with an asterisk as $\mathbf{N}^*, \mathbf{M}^*, \mathbf{T}^*$.

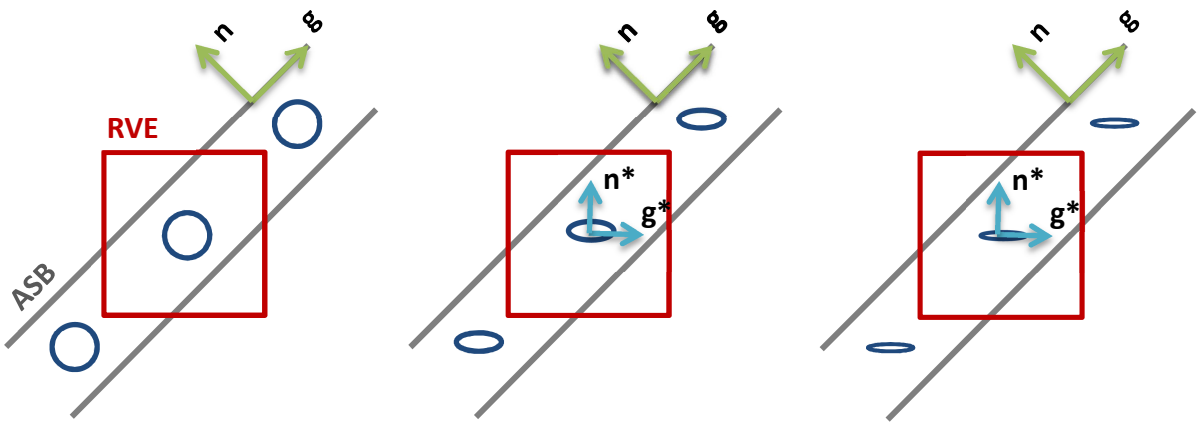

Fig. 3 Illustration of micro-void configurations. a) Spherical void configuration b) Ellipsoidal void configuration c) Micro-crack configuration.

2.1.2.3 Material consequences

As the ASB and MV are strongly oriented in space, they anisotropically degrade the elastic and plastic material properties of the RVE containing the band based on their orientation. The induced degradation may therefore be described by a 2nd order tensor variable **D** defined in (2). The components of **D** are: the scalar degradation intensities denoted by $\mathcal{D}^{ASB}, \mathcal{D}^{MV}$ and the orientation tensors $\mathbf{N},\mathbf{N}^{*}$ of ASB and MV respectively.

$$D_{ij} = \mathcal{D}_{ASB} N_{ij} + \mathcal{D}_{MV} N^{*}_{ij} \tag{2}$$

Consider the illustration in Fig. 4, the normal to the ASB and to the MV is in direction 2, in which case, the deterioration tensor is calculated below:

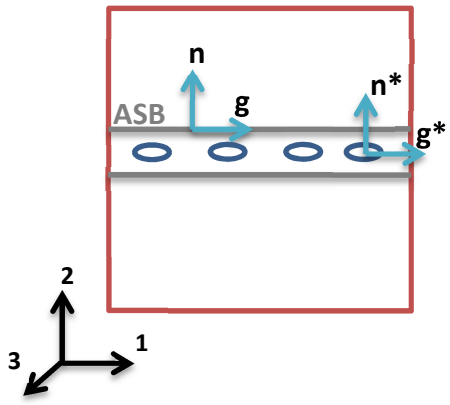

Fig. 4 Illustration ASB orientation normal to the 2 direction.

257 $$\mathbf{n}=\mathbf{n}^{*}=\begin{pmatrix}0\\1\\0\end{pmatrix}\rightarrow\mathbf{N}=\mathbf{N}^{*}=\begin{bmatrix}0&0&0\\&1&0\\sym&&0\end{bmatrix}\rightarrow\mathbf{D}=\left(\mathcal{D}^{ASB}+\mathcal{D}^{MV}\right)\begin{bmatrix}0&0&0\\&1&0\\sym&&0\end{bmatrix}\qquad(3)$$

258 According to Fig. 4, the RVE can be viewed as a 3-layer material or sandwich material
259 with a thin soft layer inserted between two thick hard layers, inducing a form of
260 orthotropy. The resulting elastic shear modulus μ_{12} and elastic axial (Young's) modulus
261 E_{22} are accordingly expected to progressively vanish while the other elastic moduli are
262 not or less affected.

263 $$\begin{cases}\tau_{12}=2\mu_{12}\left(\mathcal{D}_{ASB}\right)e^{e}_{12}\\ \tau_{22}=E_{22}\left(\mathcal{D}_{ASB}\right)e^{e}_{22}\end{cases}\ \text{with}\ \begin{cases}\begin{cases}\mu_{12}\left(\mathcal{D}_{ASB}\right)\underset{\mathcal{D}_{ASB}\rightarrow\mathcal{D}_{ASBc}}{\rightarrow}\mu_{c}\ \square\ \mu_{0}\\ E_{22}\left(\mathcal{D}_{ASB}\right)\underset{\mathcal{D}_{ASB}\rightarrow\mathcal{D}_{ASBc}}{\rightarrow}E_{c}\ \square\ E_{0}\end{cases}\rightarrow\begin{cases}\tau_{12}\left(\mathcal{D}_{ASB}\right)\underset{\mathcal{D}_{ASB}\rightarrow\mathcal{D}_{ASBc}}{\rightarrow}\tau_{12c}\\ \tau_{22}\left(\mathcal{D}_{ASB}\right)\underset{\mathcal{D}_{ASB}\rightarrow\mathcal{D}_{ASBc}}{\rightarrow}\tau_{22c}\end{cases}\\ \begin{cases}\mu_{12}\left(\mathcal{D}_{MV}\right)\underset{\mathcal{D}_{MV}\rightarrow\mathcal{D}_{MVc}}{\rightarrow}0\\ E_{22}\left(\mathcal{D}_{MV}\right)\underset{\mathcal{D}_{MV}\rightarrow\mathcal{D}_{MVc}}{\rightarrow}0\end{cases}\rightarrow\begin{cases}\tau_{12}\left(\mathcal{D}_{MV}\right)\underset{\mathcal{D}_{MV}\rightarrow\mathcal{D}_{MVc}}{\rightarrow}0\\ \tau_{22}\left(\mathcal{D}_{MV}\right)\underset{\mathcal{D}_{MV}\rightarrow\mathcal{D}_{MVc}}{\rightarrow}0\end{cases}\end{cases}\qquad(4)$$

264 where $\boldsymbol{\tau}$ is the elastic Kirchhoff stress tensor and $\mathbf{e}^{e}$ the elastic strain tensor, (μ_0, E_0)
265 and (μ_c, E_c) are the initial and critical, elastic shear and axial (Young's) moduli. Note
266 that for the case of ASB, (μ_c, E_c) have non zero values since ASB preserves matter
267 cohesion.

268 Furthermore, the effect of the combined deterioration of ASB and MV can be seen on the
269 strain hardening force $r(\kappa)$ as presented in Fig. 5. The black curve represents the strain
270 hardening solely as a function of the isotropic hardening variable κ. The blue curve
271 carries an additional influence of the temperature i.e. thermal softening. The purple
272 curve is subjected to the ASB and MV induced deterioration and hence the reduction in
273 hardening or conversely softening behaviour.

274 ***2.1.2.4 Kinematic consequences***

275 The kinematic consequences of the presence of the ASB and hence MV are viewed as
276 those of a 'macro-dislocation' considering an RVE as illustrated in Fig. 6.

277

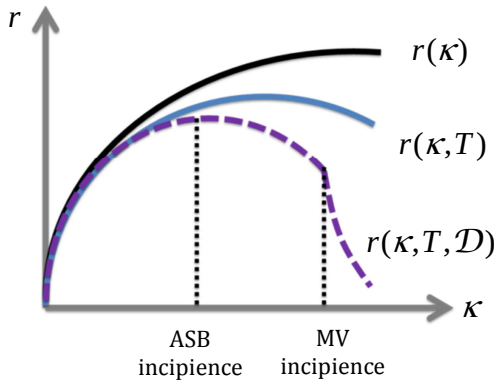

278 **Fig. 5** Strain hardening force influenced by thermal softening and ASB+MV induced deterioration

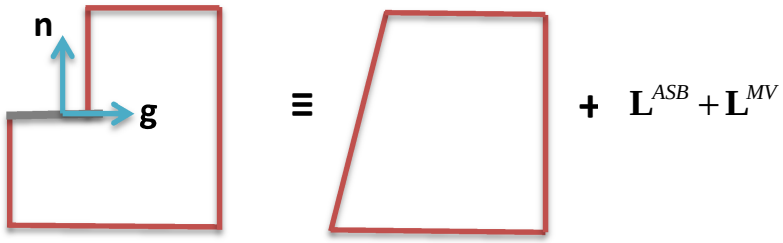

279

280 **Fig. 6** ASB viewed as a macro dislocation and the equivalent RVE with kinematic consequences. The
281 kinematic variables L^{ASB} and L^{MV} allow to smooth the boundary discontinuity caused by the ASB and
282 MV, as in crystalline plasticity and continuum damage mechanics.

283 We are designating the total velocity gradient $\mathbf{L}$ as the sum of a symmetric part $\mathbf{d}$, the
284 strain rate, and an antisymmetric part $\boldsymbol{\omega}$, the spin rate, i.e.
285 $\mathbf{L}=\mathbf{d}+\boldsymbol{\omega}$; $\mathbf{d}=\mathrm{sym}[\mathbf{L}]$; $\boldsymbol{\omega}=\mathrm{antisym}[\mathbf{L}]$. The velocity gradient created by the regular
286 plastic deformation outside the band is designated as $\mathbf{L}^{p}$. The ASB induces a
287 supplementary velocity gradient $\mathbf{L}^{ASB}$ as a result of glide velocity $\dot{\gamma}^{ASB}$ in the direction of
288 the unit vector $\mathbf{g}$; likewise the MV induced velocity gradient is termed as $\mathbf{L}^{MV}$. The
289 introduction of $\mathbf{L}^{ASB}$ and $\mathbf{L}^{MV}$ facilitates the smoothening of the boundary discontinuity
290 caused by ASB as it is done in crystalline plasticity, see Fig. 6.

291 $$\mathbf{L}^{in}=\mathbf{L}^{p}+\mathbf{L}^{ASB}+\mathbf{L}^{MV} \tag{5}$$

292 The deterioration-induced velocity gradient for a given band pattern α is partitioned
293 into symmetric and skew-symmetric parts leading to the corresponding strain rate $\mathbf{d}$
294 and spin $\boldsymbol{\omega}$ respectively as given below.

$$L_{ij}^{ASB} \propto \sum_{\alpha} \dot{\gamma}^{ASB,\alpha} g_i^{\alpha} n_j^{\alpha} \qquad \begin{cases} d_{ij}^{ASB} \propto \sum_{\alpha} \dot{\gamma}^{ASB,\alpha} M_{ij}^{\alpha} \\ \omega_{ij}^{ASB} \propto \sum_{\alpha} \dot{\gamma}^{ASB,\alpha} T_{ij}^{\alpha} \end{cases}$$

$$L_{ij}^{MV} \propto \sum_{\alpha} \dot{\gamma}^{MV,\alpha} g_i^{*\alpha} n_j^{*\alpha} + \frac{\dot{\varepsilon}_m^{MV}}{3} I_{ij} \qquad \begin{cases} d_{ij}^{MV} \propto \sum_{\alpha} \dot{\gamma}^{MV,\alpha} M_{ij}^{*\alpha} + \frac{\dot{\varepsilon}_m^{MV}}{3} I_{ij} \\ \omega_{ij}^{MV} \propto \sum_{\alpha} \dot{\gamma}^{MV,\alpha} T_{ij}^{*\alpha} \end{cases} \tag{6}$$

In case of MV configurations accounting for the void expansion, an additional hydrostatic term appears in the strain rate, where $\mathbf{I}$ is the identity tensor and $\dot{\varepsilon}_m^{MV}$ is the mean strain rate.

The kinematic consequences of the presence of ASB and MV are thus shown by the total inelastic strain rate $\mathbf{d}^{in}$ resulting from the superposition of regular plastic strain rate $\mathbf{d}^{in(PP)}$ by the singular strain rates $\mathbf{d}^{in(ASB)}$ and $\mathbf{d}^{in(MV)}$.

$$d_{ij}^{in} = d_{ij}^{in(PP)} + d_{ij}^{in(ASB)} + d_{ij}^{in(MV)} \tag{7}$$

A schematic representation of the kinematics is shown in Fig. 7 where F in all the three cases represents the plastic potential in absence of the deterioration mechanisms. Fig. 7a shows the case of regular plasticity before the appearance of ASB during which the total inelastic strain rate reduces to $\mathbf{d}^{in} = \mathbf{d}^{in(PP)} = \Gamma^{PP}\mathbf{m}$ where Γ^{PP} is the regular plastic yield intensity and $\mathbf{m}=(3/2)\,\mathrm{x}\left(\mathbf{s}/\sigma_{eq}\right)$ the yield direction (normality rule) with σ_{eq} designating Mises equivalent stress and $\mathbf{s}$ the deviatoric part of the Kirchhoff stress tensor. The ASB formation in Fig. 7b superposes an additional strain rate $\mathbf{d}^{in(ASB)} = \Gamma^{ASB}\mathbf{M}$, causing progressive deviation of the yield direction and loss of coaxiality between inelastic strain rate and stress deviator (general case). Finally, the micro-voiding in Fig. 7c further contributes to the yield intensity Γ^{MV} (assuming collinearity of ASB and MV orientations, see Fig. 4) and keeps on deviating the yield direction, provoking in particular a plastic expansion termed as $\mathrm{MV_{hydrostatic}}$.

For the different possible configurations of MV in Fig. 3, the following lists the MV induced effects:

a) The first simple configuration assumes ideal spherical voids in Fig. 3a. In this case, the spherical MV contributes to isotropic degradation ($Tr\dot{\mathbf{D}}$) and hydrostatic plastic strain rate ($\mathbf{d}_v^p$) accounting for volume change only.

b) Then the second configuration considered shows elliptical voids which possess an orientation ($\mathbf{n}^*, \mathbf{g}^*$) which may or may not be the same as that of the ASB (Fig. 3b). These types of elliptical voids contribute to anisotropic degradation rate ($\dot{\mathbf{D}} = \dot{\mathcal{D}}_{MV}\mathbf{N}^*;\ \mathbf{N}^* = \mathbf{n}^* \otimes \mathbf{n}^*$) and hydrostatic and deviatoric ($\mathbf{d}_s^p$) strain rates (with the corresponding tensor $\mathbf{M}^* = (\mathbf{g}^* \otimes \mathbf{n}^*)^S$) accounting for volume and shape changes respectively.

c) The third configuration in Fig. 3c presents micro-cracks with orientation $\mathbf{n}^*, \mathbf{g}^*$ and which influence the anisotropic degradation rate ($\dot{\mathcal{D}}_{MV}, \mathbf{N}^*$) only. When crack opening is not taken into account, there is no MV related strain rate.

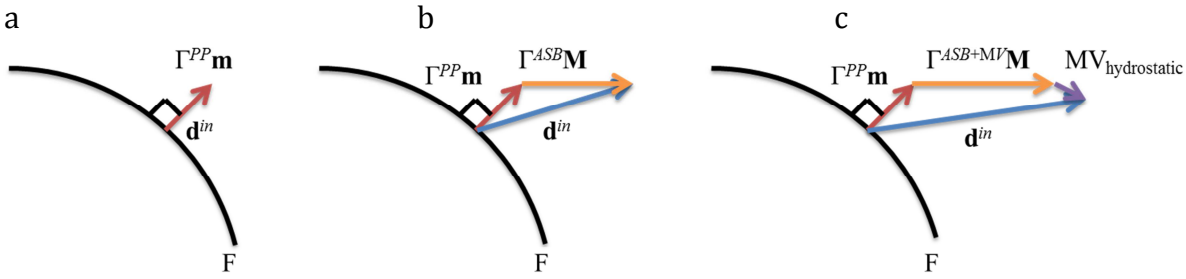

Fig. 7 Illustration of yield direction evolution (a) before ASB onset (b) during adiabatic shear banding (c) during micro-voiding. F is the regular plastic potential in the absence of deterioration mechanisms.

2.2 CONSTITUTIVE MODELLING

This section deals with the more specific form of the unified constitutive model describing the ASB and the consequent MV induced deterioration. The phenomenological model describing ASB induced failure originally developed by Longère et al [21] has been conceptually improved by Longère and Dragon [22] to incorporate the effects of micro-voiding (MV) in the post critical stage. The model used in the present work is mostly based on the enlarged model in [22] while making some simplifications/modifications. The role of dynamic recrystallization on the onset of ASB in the materials susceptible to this mechanism has also been considered here. The aim of the ASB+MV model is to clearly distinguish the contributions to the degradation coming from the ASB on the one hand and the MV on the other hand. The constitutive model presenting the dynamic recrystallization in the context of the model under consideration can be found in [30].

The constitutive model developed here is a phenomenological one wherein the consequences of the presence of the ASB at the global RVE scale on the regular properties are described. The salient physical features described by the model are:

- softening influencing ASB onset:
  - plastic dissipation induced thermal softening
  - dynamic recrystallization (DRX) induced softening
- consequences:
  - anisotropic material deterioration due to ASB+MV
  - ASB+MV induced specific finite strain kinematics

In the following, the quantities/properties associated with the material inside the ASB are termed as 'singular' and the quantities/properties associated with the material outside the band are referred to as 'regular'.

2.2.1 Large anisotropic strain framework

As very large strains and rotations are encountered during the ASB process, a finite elastic-plastic deformation framework assuming moderate elastic deformation is adopted. The objective corotational derivative $\overset{\nabla}{\mathbf{A}}$ of a 2nd order tensor $\mathbf{A}$ is given by

$$\overset{\nabla}{\mathbf{A}} = \dot{\mathbf{A}} - \mathbf{W}\mathbf{A} + \mathbf{A}\mathbf{W} \tag{8}$$

where $\mathbf{W}$ represents the rotation rate of anisotropy axes relative to ASB orientation. Taking into account the negligible elastic rotation $\boldsymbol{\omega}^{e}$ and relative small regular plastic spin $\boldsymbol{\omega}^{in(PP)}$, see [21], the rotation rate $\mathbf{W}$ is reduced to:

$$\mathbf{W} = \boldsymbol{\omega} - \left(\boldsymbol{\omega}^{in(ASB)} + \boldsymbol{\omega}^{in(MV)}\right) \tag{9}$$

where $\boldsymbol{\omega}^{in(ASB)}$ and $\boldsymbol{\omega}^{in(MV)}$ are the spin rates induced by ASB and MV respectively. In the following, the tensors $\mathbf{X}$ defined in the intermediate configuration are transported to the current one denoted by a tilde $\tilde{\mathbf{X}}$ via $\tilde{\mathbf{X}} = \mathbf{Q}\mathbf{X}\mathbf{Q}^{\mathbf{T}}$, $\mathbf{W} = \dot{\mathbf{Q}}\mathbf{Q}^{\mathbf{T}}$.

2.2.2 Thermodynamic framework

In the framework of irreversible thermodynamics, the (regular) state variables to account for are: the elastic strain tensor $\mathbf{e}^{\mathbf{e}} = \ln \mathbf{V}^{\mathbf{e}}$, the absolute temperature T, the isotropic hardening variable κ. The singular temperature and other singular state variables are not explicitly calculated in the model, but their effects on the material degradation are embodied in the degradation tensor $\tilde{\mathbf{D}}$.

Helmholtz free energy $\psi\left(\mathbf{e}^e, T, \kappa; \tilde{\mathbf{D}}\right)$ is assumed as the state potential comprising of a reversible part $\psi^e\left(\mathbf{e}^e, T; \tilde{\mathbf{D}}\right)$, a stored energy part $\psi^p\left(T, \kappa; \tilde{\mathbf{D}}\right)$ and a purely thermal part $\psi^T(T)$ as shown in (10). The presence of ASB affects both the elastic and plastic properties.

$$\psi\left(\mathbf{e}^e, T, \kappa; \tilde{\mathbf{D}}\right) = \psi^e\left(\mathbf{e}^e, T; \tilde{\mathbf{D}}\right) + \psi^p\left(T, \kappa; \tilde{\mathbf{D}}\right) + \psi^T(T) \tag{10}$$

Constitutive state laws derived from the state potential in (10) allows for expressing the elastic Kirchhoff stress tensor $\boldsymbol{\tau}$, strain hardening force r, deterioration driving force $\tilde{\mathbf{G}}$ and entropy s, as follows:

$$\begin{aligned}
&\tau_{ij} = \rho_0 \frac{\partial \psi}{\partial e^e_{ij}} = \rho_0 \frac{\partial \psi^e}{\partial e^e_{ij}} \;;\; r = \rho_0 \frac{\partial \psi}{\partial \kappa} = \rho_0 \frac{\partial \psi^p}{\partial \kappa} \\
&\tilde{G}_{ij} = -\rho_0 \frac{\partial \psi}{\partial \tilde{D}_{ij}} = -\left(\rho_0 \frac{\partial \psi^e}{\partial \tilde{D}_{ij}} + \rho_0 \frac{\partial \psi^p}{\partial \tilde{D}_{ij}} \right) \\
&\rho_0 s = -\rho_0 \frac{\partial \psi}{\partial T} = -\left(\rho_0 \frac{\partial \psi^e}{\partial T} + \rho_0 \frac{\partial \psi^p}{\partial T} + \rho_0 \frac{d\psi^T}{dT} \right)
\end{aligned} \tag{11}$$

where ρ_0 designates the initial mass density. The model should satisfy the Clausius-Duhem inequality in order to be consistent with the irreversible thermodynamics. Therefore the intrinsic dissipation $\mathcal{D}_{\text{int}}$ is expressed as:

$$\mathcal{D}_{\text{int}} = \tau_{ij} d_{ji} - \rho_0 (\dot{\psi} + s\dot{T}) \geq 0 \tag{12}$$

$\mathcal{D}_{\text{int}}$ is decomposed into regular plasticity related term $\mathcal{D}_{reg}$ and singular ASB+MV induced term $\mathcal{D}_{\mathbf{sing}}$. Using the Gibbs relation $\rho_0 \dot{\psi} = \tau_{ij} d^e_{ij} + r\dot{\kappa} - \tilde{G}_{ij} \dot{\tilde{D}}_{ij} - \rho_0 s\dot{T}$ the dissipation components are written as:

$$\begin{aligned}
&\mathcal{D}_{\text{int}} = \mathcal{D}_{\text{reg}} + \mathcal{D}_{\text{sing}} \geq 0 \\
&\mathcal{D}_{\text{reg}} = \tau_{ij} d^p_{ji} - r\dot{\kappa} \geq 0 \;;\; \mathcal{D}_{\text{sing}} = \tau_{ij} d^d_{ji} + \tilde{G}_{ij} \overset{\nabla}{\tilde{D}}_{ji} \geq 0
\end{aligned} \;;\; \begin{cases} d^p_{ij} = d^{in(PP)}_{ij} \\ d^d_{ij} = d^{in(ASB)}_{ij} + d^{in(MV)}_{ij} \end{cases} \tag{13}$$

In the context of generalised normality rule, the evolutions laws are correspondingly derived from dissipation potentials namely the viscoplastic potential ϕ_p and viscous-degradation potential $\phi_d = \phi_{ASB} + \phi_{MV}$ as:

$$d_{ij}^{in} = \frac{\partial \phi_p}{\partial \tau_{ij}} = d_{ij}^{in(PP)} + d_{ij}^{in(ASB)} + d_{ij}^{in(MV)}$$

$$-\dot{\kappa} = \frac{\partial \phi_p}{\partial r} \tag{14}$$

$$\overset{\nabla}{\tilde{D}}_{ij} = \frac{\partial \phi_d}{\partial G_{ij}} = \overset{\nabla}{\tilde{D}}_{ij}^{ASB} + \overset{\nabla}{\tilde{D}}_{ij}^{MV}$$

It is now required to define a plastic potential H and/or a yield function F depending on whether non-associated ($H \neq F$) or associated flow rule ($H = F$) is followed.

2.2.3 Constitutive equations

A more precise form of the constitutive equations adopted in the current study is presented in this section. In the following, for simplification, elliptical void shape is assumed with the orientation along the direction of the ASB as represented in Fig. 8. Hence the structural tensors in (1) corresponding to the ASB and MV are considered to be the same ($\mathbf{N}, \mathbf{M}$).

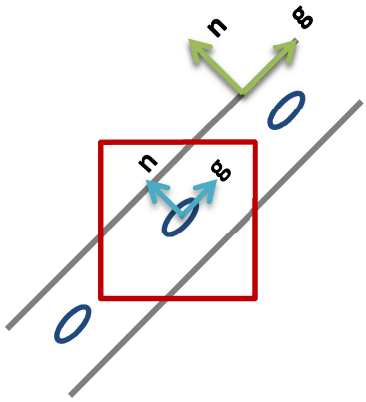

Fig. 8 Elongated micro-voids oriented in the direction of ASB

2.2.3.1 Preliminary considerations

- *Elastic stress tensor*

Following the work of Halm and Dragon [31], see also Longère and Dragon [21], the elastic stress tensor in presence of anisotropic damage induced degradation is assumed of the form:

410 $$\tau_{ij} = \rho_0 \frac{\partial \psi}{\partial e^e_{ij}} = \rho_0 \frac{\partial \psi^e}{\partial e^e_{ij}} = \lambda e^e_{kk} I_{ij} + 2\mu e^e_{ij} - \bar{\alpha} K \Delta T \, I_{ij} - a\left(e^e_{mn}\tilde{D}_{nm} I_{ij} + e^e_{kk}\tilde{D}_{ij}\right) - 2b\left(e^e_{ik}\tilde{D}_{kj} + \tilde{D}_{ik}e^e_{kj}\right)$$

411 (15)

412 The form given to the stress tensor in (15) is such that it takes into account material
413 degradation based on the orientation of the shear bands. λ and μ represent the Lamé
414 elasticity constants and $K = (3\lambda + 2\mu)/3$ the bulk modulus. a and b are ASB+MV related
415 constants inducing orthotropic elastic energy degradation – they may have different
416 values for ASB and MV in a future work. In the thermal part, $\bar{\alpha}$ represents the thermal
417 expansion coefficient, T_0 the initial temperature and $\Delta T = T - T_0$ the rise in temperature.

418 Consider now the illustration in Fig. 4, the normal to the ASB is in direction 2, in which
419 case, the deterioration tensor is calculated below:

420 $$\mathbf{n} = \begin{pmatrix} 0 \\ 1 \\ 0 \end{pmatrix} \rightarrow \mathbf{D} = \mathcal{D} \begin{bmatrix} 0 & 0 & 0 \\ & 1 & 0 \\ sym & & 0 \end{bmatrix} ; \; \mathcal{D} = \mathcal{D}^{ASB} + \mathcal{D}^{MV} \qquad (16)$$

421 By neglecting the thermal dilatation, the components of $\boldsymbol{\tau}$ for the above case (Fig. 4)
422 deduced from (15)-(16) are:

423 $$\begin{cases} \tau_{11} = (\lambda + 2\mu) e^e_{11} + \left(\lambda - a\tilde{D}_{22}\right) e^e_{22} + \lambda e^e_{33} \\ \tau_{22} = \left(\lambda - a\tilde{D}_{22}\right)\left(e^e_{11} + e^e_{33}\right) + \left[\left(\lambda - 2a\tilde{D}_{22}\right) + 2\left(\mu - 2b\tilde{D}_{22}\right)\right] e^e_{22} \\ \tau_{33} = (\lambda + 2\mu) e^e_{33} + \left(\lambda - a\tilde{D}_{22}\right) e^e_{22} + \lambda e^e_{11} \end{cases} \qquad (17)$$

424 $$\begin{cases} \tau_{12} = 2\left(\mu - b\tilde{D}_{22}\right) e^e_{12} \\ \tau_{13} = 2\mu e^e_{13} \\ \tau_{23} = 2\left(\mu - b\tilde{D}_{22}\right) e^e_{23} \end{cases}$$

425 The resulting (symmetric) stiffness matrix $\mathbf{C}$, $\boldsymbol{\tau} = \mathbf{C} : \mathbf{e}^e$, reads

$$[C]=\begin{bmatrix} \lambda+2\mu & (\lambda-a\mathcal{D}) & \lambda & 0 & 0 & 0 \\ & (\lambda-2a\mathcal{D})+2(\mu-2b\mathcal{D}) & (\lambda-a\mathcal{D}) & 0 & 0 & 0 \\ & & \lambda+2\mu & 0 & 0 & 0 \\ & & & 2(\mu-b\mathcal{D}) & 0 & 0 \\ & & & & 2\mu & 0 \\ sym & & & & & 2(\mu-b\mathcal{D}) \end{bmatrix} \quad (18)$$

Failure under shear loading yields an upper bound for deterioration intensity $\mathcal{D}_c$ as shown below:

$$\tau_{12}=2(\mu-b\mathcal{D}_c)e^e_{12}=0 \quad \rightarrow \quad \mathcal{D}_c=\frac{\mu}{b}\rightarrow \mathcal{D}_c(b=\mu)=1 \quad (19)$$

A reduction in the material strength is seen in the direction normal to the ASB (τ_{22}) and in the corresponding shear direction (τ_{12}). It is seen that the constants $a<0$ and $b>0$ contribute to the reduction in Young's modulus E_{22} whereas only b acts in the reduction of the shear modulus μ_{12}.

- *Strain hardening force*

Experimental observations have shown that in absence of ASB and MV the coupling between strain hardening and thermal softening may be described in a product form allowing for using the method of separation of variables

$$r(\kappa,T)=\rho_0\frac{\partial\psi}{\partial\kappa}=\rho_0\frac{\partial\psi^p}{\partial\kappa}=h'(\kappa)g(T) \quad (20)$$

The form of the thermal softening corresponding to steel is shown in (21) where υ is the material specific thermal softening constant

$$g(T)=\exp(-\upsilon T) \quad (21)$$

For materials such as titanium alloys, in accordance with experimental observations, the function in (22) satisfies the thermal softening characteristics with T_{ref} being a reference temperature such that $g(T_{ref})=0$. $\langle.\rangle$ are Macauley brackets defined as $\langle x\rangle=\max(x,0)$.

$$g(T)=\left\langle 1-\left(\frac{T}{T_{ref}}\right)^{t}\right\rangle \tag{22}$$

where t designates a constant. The strain hardening function is expressed in (23) where R_∞ is related to the saturation of isotropic hardening (Voce law).

$$h'(\kappa)=R_\infty\left[1-\exp\left(-k\kappa\right)\right];h(\kappa)=R_\infty\left[\kappa+\frac{1}{k}\exp\left(-k\kappa\right)\right] \tag{23}$$

We are here assuming that this product form can be extended for ASB and MV

$$r\left(\kappa,T;\tilde{\mathbf{D}}\right)=\rho_0\frac{\partial\psi}{\partial\kappa}=\rho_0\frac{\partial\psi^p}{\partial\kappa}=h'\left(\kappa\right)g\left(T\right)w\left(\tilde{\mathbf{D}}\right) \tag{24}$$

In the following equations the thermal softening function in (21) is used. The deterioration function $w(\tilde{\mathbf{D}})$ is expressed below where χ_1 and χ_2 are ASB+MV related deterioration constants. The form of the deterioration function $w(\tilde{\mathbf{D}})$ is adopted of the same exponential form as the thermal softening function in (21) as the singular temperature rise within the shear band is the main contributor to the material deterioration. The expression of $w(\tilde{\mathbf{D}})$ in (25) is tentatively retained for other materials such as Ti alloys even though the form of their thermal softening function is different.

$$w(D_{ij})=\exp\left(-\chi_1\tilde{D}_{ii}-\frac{\chi_2}{2}\tilde{D}_{ij}\tilde{D}_{ji}\right) \tag{25}$$

2.2.3.2 State potential

According to the preliminary considerations above, the state potential reads after integration of the constitutive state laws in (15) and (24) with respect to their different arguments:

$$\psi\left(\mathbf{e}^e,T,\kappa;\tilde{\mathbf{D}}\right)=\psi^e\left(\mathbf{e}^e,T;\tilde{\mathbf{D}}\right)+\psi^p\left(T,\kappa;\tilde{\mathbf{D}}\right)+\psi^T\left(T\right)$$

$$\begin{cases}\rho_0\psi^e\left(\mathbf{e}^e,T;\tilde{\mathbf{D}}\right)=\frac{1}{2}\mathbf{e}^e:\mathbf{C}(\tilde{\mathbf{D}}):\mathbf{e}^e-\bar{\alpha}K.Tr(\mathbf{e}^e).\Delta T\\ \rho_0\psi^p\left(T,\kappa;\tilde{\mathbf{D}}\right)=h(\kappa)g(T)w(\tilde{\mathbf{D}})\\ \rho_0\psi^T\left(T\right)=-\rho_0\frac{C}{2T_0}\Delta T^2\end{cases} \tag{26}$$

where C designates the specific heat.

2.2.3.3 Constitutive state laws

The complete expressions of the conjugate forces associated to the state variables, considering steel oriented thermal softening function, is shown below:

$$\begin{cases} \tau_{ij} = \lambda e^e_{kk} I_{ij} + 2\mu e^e_{ij} - \bar{\alpha} K \Delta T\, I_{ij} - a\left(e^e_{mn}\tilde{D}_{nm} I_{ij} + e^e_{kk}\tilde{D}_{ij}\right) - 2b\left(e^e_{ik}\tilde{D}_{kj} + \tilde{D}_{ik}e^e_{kj}\right) \\ r = R_\infty\left[1-\exp\left(-k\kappa\right)\right]\exp\left(-\upsilon T\right)\exp\left(-\chi_1\tilde{D}_{kk} - \frac{\chi_2}{2}\tilde{D}_{kl}\tilde{D}_{lk}\right) \\ \tilde{G}_{ij} = a e^e_{kk} e^e_{ij} + 2b e^e_{ik} e^e_{kj} + R_\infty\left[\kappa + \frac{1}{k}\exp\left(-k\kappa\right)\right] \\ \qquad .\exp\left(-\upsilon T\right)\exp\left(-\chi_1\tilde{D}_{kk} - \frac{\chi_2}{2}\tilde{D}_{kl}\tilde{D}_{lk}\right)\left[\chi_1 I_{ij} + \chi_2\tilde{D}_{ij}\right] \end{cases} \tag{27}$$

The expression of the entropy is not detailed here. The diminution of the stress $\boldsymbol{\tau}$ is caused by the isotropic heating and ASB+MV induced anisotropic degradation. The competition between hardening and softening is embodied in the isotropic hardening conjugate force r: the strain hardening capability $\partial r/\partial\kappa$ is decreased by the thermal softening function $g(T)$. In addition, as the deterioration $\mathbf{D}$ evolves, the deterioration related function $w(\tilde{\mathbf{D}})$ magnifies the loss of the strain hardening capability as illustrated in Fig. 5. In isothermal conditions and in the absence of deterioration, r reaches a saturation stress $R_\infty\exp\left(-\upsilon T_0\right)$ relative to isotropic hardening. The deterioration conjugate force $\tilde{\mathbf{G}}$ has contributions from the reversible part ψ^e and stored energy part ψ^p of the free energy which correspondingly represent the elastic and stored energy release rate. $\tilde{\mathbf{G}}$ in the following is contained in ΔG_{ASB} and ΔG_{MV} through the scalar quantity G obtained by the projection of $\tilde{\mathbf{G}}$ onto the band plane. In particular, the values of G at the ASB and MV onset are considered namely G_{ASB} and G_{MV} respectively and the quantities ΔG_{ASB} and ΔG_{MV} which are defined as:

$$G = \tilde{G}_{ij}N_{ji}\ ;\ \Delta G_{ASB} = \left\langle G - G_{ASB}\right\rangle\ ;\ \Delta G_{MV} = \left\langle G - G_{MV}\right\rangle \tag{28}$$

It is to be noted that the deterioration conjugate force exists and evolves even before the deterioration onset. A finite supply of local energy release rate (G_{ASB}, G_{MV}) is required to activate the deterioration (ASB, MV). The deterioration onset criteria and calculation of G_{ASB} and G_{MV} are defined in section 2.3.

2.2.3.4 Yield function

Various void induced damage models exist in the literature. Lemaitre [32] modelled ductile damage considering non-dilatant effect of void growth. The dilatant void growth models of Rousselier [33] and GTN (Gurson-Tvergaard-Needleman) ([34],[35]) are widely used damage plasticity models to describe ductile damage. The ASB induced degradation, in the present study, was initially described using a thermo/elastic-viscoplastic-deterioration (TEVPD) model. Now, in order to describe the post critical micro-voiding, rather than using another plasticity–ductile damage coupled model, a 'unified approach' is adopted wherein the MV induced consequences are merged within the TEVPD framework without distorting much its formal structure. The unified enlarged model has some analogies with Rousselier model [33] for its dependence on hydrostatic stress via an exponential function that notably allows for reproducing void growth under shear loading.

The yield function F_{total} when both the ASB and MV mechanisms are in operation reads:

$$\mathrm{F}_{total} = \sigma_{eq} + 3\xi\,\Delta G_{MV}^{2}\exp\left(\frac{\sigma_m}{\bar{\sigma}}\right) - \left(R_0 + r\right) = \sigma_v \geq 0 \tag{29}$$

where σ_{eq} is the transformed equivalent stress accounting for the anisotropy induced in the plastic flow by evolving ASB and MV, $\left(R_0 + r\right)$ the rate independent yield stress with r the strain hardening force, σ_v the strain rate induced overstress, $\sigma_m = \tau_{kk}/3$ the mean stress and $\bar{\sigma}$ a reference stress. R_0 is expressed in (30) with R_{int} being the internal stress (thermal softening function related to steel).

$$R_0 = R_{\mathrm{int}}\exp(-\upsilon T)\exp\left(-\chi_1\tilde{D}_{kk} - \frac{\chi_2}{2}\tilde{D}_{kl}\tilde{D}_{lk}\right) \tag{30}$$

The second term of the expression of F_{total} containing σ_m corresponds to the expansion of micro-voids with ξ being the related material constant. The ΔG_{MV} in this term has been modified to ΔG_{MV}^{2} from the previous work ([22],[36],[37]) in order to be consistent with the MV incipience while deriving the deterioration rate expressed in $(39)_2$ below.

2.2.3.5 Equivalent stress

As mentioned above, a transformed equivalent stress σ_{eq} is used here which incorporates the regular plasticity and the anisotropy induced in the plastic flow provoked by the formation (onset and evolution) of the strongly oriented deterioration mechanisms at stake (ASB+MV) through a 4th order tensor $\mathbf{P}$ as shown below:

$$\sigma_{eq} = \sqrt{\frac{3}{2}\mathbf{s}:\mathbf{P}\left(\Delta G_{ASB}, \Delta G_{MV}\right):\mathbf{s}} \; ; \; \mathbf{P} = \mathbf{I} + 2\left(\eta_{ASB}\Delta G_{ASB}^2 + \eta_{MV}\Delta G_{MV}^2\right)\mathbf{M}\otimes\mathbf{M} \qquad (31)$$

where $\mathbf{s}$ is the deviatoric part of the Kirchhoff stress tensor, $\mathbf{I}$ the 4th order identity tensor, $\mathrm{I}_{ijkl} = \frac{1}{2}\left(\delta_{ik}\delta_{jl} + \delta_{il}\delta_{jk}\right)$, and η_{ASB} and η_{MV} material constants relative to the corresponding mechanisms. A power of 2 is used for ΔG_{ASB} and ΔG_{MV} terms, see their definitions in (28), in the above expression in order to ensure the concomitance of the deterioration induced rates while deriving their expressions later in (37) and (39) below. The transformed equivalent stress σ_{eq} in (31) may also be expressed of the form:

$$\sigma_{eq} \equiv \sqrt{{\sigma_{VM}}^2 + {\sigma_{ASB}}^2 + {\sigma_{MV}}^2} \; ; \begin{cases} \sigma_{VM} = \sqrt{\frac{3}{2}\mathbf{s}:\mathbf{s}} \\ \sigma_{ASB} = \sqrt{3\eta_{ASB}}\Delta G_{ASB}\tau_{res} \\ \sigma_{MV} = \sqrt{3\eta_{MV}}\Delta G_{MV}\tau_{res} \end{cases} \qquad (32)$$

where $\tau_{res} = \left|\mathbf{s}:\mathbf{M}\right|$ represents the shear stress resolved along the band plane. σ_{eq} in (32) therefore has contributions from the regular and singular mechanisms and is composed of the regular plastic von Mises equivalent stress σ_{VM} and the singular stresses induced by ASB - σ_{ASB} and then by MV- σ_{MV}.

One can note that, in the absence of MV ($\Delta G_{MV} = 0$), F_{total} in (29) reduces to F_{PP+ASB} i.e. yield function in the presence of ASB only. Further in the absence of ASB ($\Delta G_{ASB} = 0$), Von Mises yield criterion F_{PP} is followed. The different possible cases of the yield function in the presence or absence of ASB and MV are shown in Table 1.

The expressions for the singular contributions to the equivalent stress are modified here from the earlier versions in order to take into account the loss of strength of the material due to ASB and the subsequent MV in the direction normal to the band during tension loading by adding the stress term $\sigma_N = \left\langle \boldsymbol{\tau}:\mathbf{N} \right\rangle = \max\left(0, \boldsymbol{\tau}:\mathbf{N}\right)$ in the expression of the transformed equivalent stress:

$$\hat{\sigma}_{eq} \equiv \sqrt{{\sigma_{VM}}^2 + {\hat{\sigma}_{ASB}}^2 + {\hat{\sigma}_{MV}}^2}\ ; \begin{cases} \hat{\sigma}_{ASB} = \sqrt{\eta_{ASB}\left(3\tau_{res}^2 + \alpha\sigma_N^2\right)}\Delta G_{ASB} \\ \hat{\sigma}_{MV} = \sqrt{\eta_{MV}\left(3\tau_{res}^2 + \alpha\sigma_N^2\right)}\Delta G_{MV} \end{cases} \tag{33}$$

$$\mathrm{F}_{total} = \hat{\sigma}_{eq}\left(\mathbf{s}, \Delta G_{ASB}, \Delta G_{MV}\right) + 3\xi\,\Delta G_{MV}^2 \exp\left(\frac{\sigma_m}{\bar{\sigma}}\right) - \left(R_0 + r\right) = \sigma_v \geq 0$$

Table 1 Form of yield function in the presence or absence of ASB and MV

Operating Mechanisms	ΔG	${\sigma_{eq}}^2$	$\mathrm{F} = \sigma_v \geq 0$
$PP + ASB + MV$	$\Delta G_{ASB} \neq 0$ $\Delta G_{MV} \neq 0$	${\sigma_{VM}}^2 + {\sigma_{ASB}}^2 + {\sigma_{MV}}^2$	$\mathrm{F}_{total} = \sigma_{eq}\left(\mathbf{s}, \Delta G_{ASB}, \Delta G_{MV}\right) + 3\xi\,\Delta G_{MV}^2 \exp\left(\frac{\sigma_m}{\bar{\sigma}}\right) - \left(R_0 + r\right)$
$PP + ASB$	$\Delta G_{ASB} \neq 0$ $\Delta G_{MV} = 0$	${\sigma_{VM}}^2 + {\sigma_{ASB}}^2$	$\mathrm{F}_{PP+ASB} = \sigma_{eq}\left(\mathbf{s}, \Delta G_{ASB}, 0\right) - \left(R_0 + r\right)$
PP	$\Delta G_{ASB} = 0$ $\Delta G_{MV} = 0$	${\sigma_{VM}}^2$	$\mathrm{F}_{PP} = \sigma_{eq}\left(\mathbf{s}, 0, 0\right) - \left(R_0 + r\right)$

The value of the coefficient α is assigned 3 in the present work. The scalar function preceding $\mathbf{M} \otimes \mathbf{M}$ in the original expression of $\mathbf{P}$ (see equation (36) in [22]) has been limited here to a single term. In a certain way, the a posteriori addition of σ_N in the transformed equivalent stress allows for palliating the aforementioned truncation. During tension loading in the direction normal to the shear band, presumably the entire load is carried by the shear bands. During normal compression loading, when $\tau_{res} = 0$ and $\sigma_N = 0$, the RVE is supposed to contain no shear bands and the entire load is carried by the regular matrix material.

It is to be remarked that ASB induced deterioration is in operation during the loading duration when the shear band is still soft. With longer duration or during interrupted loading, the material within the ASB would possibly undergo phase transformation due to quenching by the surrounding regular material and become harder. In this case, the material regains its near original strength except for the irreversible MV deterioration. This remark is to be taken into account in the prospective work.

2.2.3.6 Viscoplastic and viscous-damage potential

The existence of viscoplastic potential ϕ_p and viscous-deterioration potential ϕ_{ASB}, ϕ_{MV} of Norton-Perzyna's type is assumed in the form of power law:

559 $$\phi_p = \frac{Y}{n+1}\left\langle \frac{\mathrm{H}}{Y} \right\rangle^{n+1} \;;\; \phi_{ASB} = \frac{Z}{m+1}\left\langle \frac{\mathrm{H}}{Z} \right\rangle^{m+1} \;;\; \phi_{MV} = \frac{W}{q+1}\left\langle \frac{\mathrm{H}}{W} \right\rangle^{q+1} \tag{34}$$

560 Y and n are viscous constants corresponding to the regular plasticity; Z, m and W, q
561 are time-dependence related constants corresponding to the ASB and MV degradation
562 mechanisms respectively.

563 ***2.2.3.7 Evolution laws***

564 A non-associated plasticity is followed such that the plastic potential $\mathrm{H} = \mathrm{F}_{total}\left(\sigma_N \equiv 0\right)$
565 as expressed below.

566 $$\mathrm{H} = \sigma_{eq} + 3\xi\,\Delta G_{MV}^2 \exp\left(\frac{\sigma_m}{\bar{\sigma}}\right) - \left(R_0 + r\right) \tag{35}$$

567 The viscoplastic multiplier Λ_p and viscous-deterioration multipliers Λ_{ASB}, Λ_{MV} are
568 expressed below.

569 $$\Lambda_p = \left\langle \frac{\partial \phi_p}{\partial F} \right\rangle = \left\langle \frac{\mathrm{H}}{Y} \right\rangle^n \;;\; \Lambda_{ASB} = \left\langle \frac{\partial \phi_d}{\partial F} \right\rangle = \left\langle \frac{\mathrm{H}}{Z} \right\rangle^m \;;\; \Lambda_{MV} = \left\langle \frac{\partial \phi_d}{\partial F} \right\rangle = \left\langle \frac{\mathrm{H}}{W} \right\rangle^q \tag{36}$$

570 The detailed rate equations derived from the plastic potential according to the normality
571 rule are shown below. In addition to the deviatoric component, the MV induced strain
572 rate $\mathbf{d}^{in(MV)}$ is also composed of a hydrostatic component. The MV expansion described
573 by the dependence on the mean stress according to $\exp(\sigma_m / \bar{\sigma})$ was initially proposed by
574 Rice and Tracey [38].

575 $$\begin{cases} d_{ij}^{in(PP)} = \dfrac{3}{2}\Lambda_P \dfrac{s_{ij}}{\sigma_{eq}} \\ d_{ij}^{in(ASB)} = 3\Lambda_P \dfrac{\eta_{ASB}\Delta G_{ASB}^2 \tau_{res}}{\sigma_{eq}} M_{ij} \\ d_{ij}^{in(MV)} = 3\Lambda_P \left[\dfrac{\eta_{MV}\Delta G_{MV}^2 \tau_{res}}{\sigma_{eq}} M_{ij} + \dfrac{\xi}{3\bar{\sigma}} \Delta G_{MV}^2 \exp\left(\dfrac{\sigma_m}{\bar{\sigma}}\right) I_{ij} \right] \end{cases} \tag{37}$$

576 $$\dot{\kappa} = \Lambda_p \tag{38}$$

577
$$\begin{cases} \overset{\nabla}{D}_{ij}^{ASB} = \dfrac{3\tau_{res}^2}{\sigma_{eq}} \Lambda_{ASB} \eta_{ASB} \Delta G_{ASB} N_{ij} \\ \overset{\nabla}{D}_{ij}^{MV} = 3\Lambda_{MV} \left[\dfrac{\tau_{res}^2}{\sigma_{eq}} \eta_{MV} \Delta G_{MV} + 2\xi \Delta G_{MV} \exp\left(\dfrac{\sigma_m}{\bar{\sigma}} \right) \right] N_{ij} \end{cases} \quad (39)$$

578 It is to be noted that in the present study void expansion is modelled irreversibly and the
579 void closure which may take place during change of the loading sign is not taken into
580 consideration. The inclusion of ΔG_{MV}^2 in the void expansion term of the yield function
581 translates into ΔG_{MV}^2 and ΔG_{MV} in the corresponding terms of $d_{ij}^{in(MV)}$ and $\overset{\nabla}{D}_{ij}^{MV}$
582 respectively. This ensures the systematic concomitance of the deviatoric and hydrostatic
583 terms of the rate equation relevant to MV.

584 The components of the deterioration induced spin rates can be deduced from (6) and
585 (37) as:

586
$$\begin{aligned} \omega_{ij}^{in(ASB)} &= 3\Lambda_P \frac{\eta_{ASB} \Delta G_{ASB}^2 \tau_{res}}{\sigma_{eq}} T_{ij} \\ \omega_{ij}^{in(MV)} &= 3\Lambda_P \frac{\eta_{MV} \Delta G_{MV}^2 \tau_{res}}{\sigma_{eq}} T_{ij} \end{aligned} \quad (40)$$

587 ***2.2.3.8 Viscous stress***

588 The viscous stress in (35) is assumed of the form:

589
$$\sigma_v = Y \dot{\kappa}^{1/n} \quad (41)$$

590 It is reminded that Y and n are viscous constants corresponding to the regular plasticity
591 and as such do not depend on D.

592 ***2.2.3.9 Temperature rise***

593 The regular temperature rate is calculated from the intrinsic plastic dissipation
594 expressed in (13) assuming adiabatic conditions as:

595
$$\rho c \dot{T} = \tau_{ij} : d_{ji}^p - r\dot{\kappa} \quad (42)$$

As the dissipation progressively concentrates within the band during the ASB process, the regular temperature rate accordingly vanishes and the regular temperature saturates; further cooling during unloading should be accounted for in prospective works.

2.3 DETERIORATION INCIPIENCE CRITERIA

The mechanisms leading to onset of the ASB and MV and the corresponding criteria adopted are discussed in the current section.

2.3.1 Softening mechanisms triggering the ASB formation

A criterion for the incipience of the ASB based on the physics of the mechanism is essential. In the literature, several arbitrary ASB incipience criteria have been postulated for example based on critical strain, see Zhou et al. [39], strain rate, see Bonnet-Lebouvier et al. [14], temperature rise, see Teng et al. [15], and energy, see Dolinski et al. [40]. Although the above mentioned engineering oriented criteria are easy to implement, they strongly depend on the geometry and loading conditions. Hence there is a need for a robust physics based criterion consistent with the constitutive equations. Such a criterion may be obtained from the linear perturbation analysis, see e.g. Anand et al. [41]. Longère et al. developed a criterion as shown in (43) based on simplified analysis of material instability accounting for the competition between hardening and softening mechanisms using the linear perturbation method. A detailed account of this approach can be consulted in the references - Molinari [42], Longère et al. [21], Longère and Dragon [43].

$$\mathrm{J}\left(\tau_{ij}, r, \dot{\kappa}; \frac{\partial r}{\partial \kappa}, \frac{\partial r}{\partial T}\right) = \sqrt{3}\tau - \left(r - \frac{1}{n} Y \dot{\kappa}^{\frac{1}{n}} + \rho_0 c_0 \left(\frac{\partial r}{\partial \kappa} \Big/ \left(-\frac{\partial r}{\partial T}\right)\right)\right) \geq 0 \qquad (43)$$

where $\partial r / \partial \kappa$ represents the strain hardening and $\partial r / \partial T$ the thermal softening effects. The deterioration process is actually assumed to run as soon as $\mathrm{J} = 0$. This criterion allows for determining G_{ASB} (= $\mathbf{G} : \mathbf{N}$ at the instant of ASB incipience).

Two softening mechanisms triggering the ASB formation are considered in the present study, viz. thermal softening and dynamic recrystallization.

2.3.1.1 Thermal softening

At high strain rates, adiabatic conditions can be assumed due to the limited time for heat transfer (see [44]). Thermal softening along with quasi-adiabatic condition plays an important role in provoking the ASB onset. The form of the thermal softening function can be adapted to different materials as shown in (21) and (22). It is therefore essential to accurately calculate the regular temperature rise causing the thermal softening. The plasticity induced regular temperature rise shown in (42) can also be expressed as:

$$\rho c\dot{T} = \left(\frac{\sigma_{VM}^2}{\sigma_{eq}} - r \right) \dot{\kappa} \tag{44}$$

In most studies in the literature, the percentage of plastic work converted to heat i.e. the inelastic heat fraction β is assumed to be constant; for example $\beta = 0.6$ in [45], $\beta = 0.9$ in [46]. However the experiments by Mason et al. [47] show that β is not a constant and varies with the strain, strain rate and temperature (see also [48],[49]) as is potentially the case in the present study. The form of the inelastic heat fraction can be deduced from (44) as:

$$\rho c\dot{T} = \beta \sigma_{VM} \dot{\kappa} \quad ; \quad \beta = \frac{\sigma_{VM}}{\sigma_{eq}} - \frac{r}{\sigma_{VM}} \tag{45}$$

As r depends on strain and temperature and σ_{VM} is a function of strain, strain rate and temperature, β is expected to depend on strain, strain rate and temperature as well, see [50]. During the ASB process, the dissipation progressively concentrates within the bands. Correspondingly, the evolution of the regular temperature outside the bands diminishes and finally saturates.

2.3.1.2 Dynamic recrystallization

It has been shown that the microstructure also influences the ASB incipience, see eg. Liu et al. [28]. The micro-mechanisms contributing to the regular material softening and influencing the ASB onset, which are taken into consideration in the present study, are the dynamic recovery (DRC) and dynamic recrystallization (DRX). Many studies have shown that the DRX occurs as a consequence of the adiabatic shear banding ([51],[52],[53]). Contrarily, for certain alloys such as those of titanium, DRX is shown to contribute significantly to the softening leading to the very formation of ASB (see [25],[26]). The latter approach is considered in the present work and the competition between the DRX softening and thermal softening provoking the ASB initiation is

studied. The detailed development of the DRX related model can be found in the article by Longère [30].

For the initial study on DRX, a critical value of the isotropic hardening variable κ_c is imposed to initiate occurrence of DRX. According to Mohamed and Bacroix [54], the stored energy at DRX onset should depend on temperature. But in the present study, for simplification, κ_c is maintained constant and temperature independent. The DRC and DRX induce a negative hardening effect (softening) and it is modelled in the hardening term $h'(\kappa)$ as shown in (46).

$$h'(\kappa) = \tau_s\left(Y(\kappa)\right)\left[1-\exp\left(-\frac{Y(\kappa)}{2}\kappa\right)\right] \tag{46}$$

τ_s is the DRC and DRX dependent saturation value of hardening stress. $Y(\kappa)$ is a non-dimensional quantity phenomenologically composed of DRC and DRX components expressed below.

$$Y(\kappa) = Y_{DRC} + Y_{DRX}(\kappa); \qquad \tau_s\left(Y(\kappa)\right) = \frac{\eta}{Y(\kappa)} \tag{47}$$

where

$$\begin{cases} Y_{DRC} = Y_0 \\ Y_{DRX} = Y_{\max}\left[1-\exp\left(-\dfrac{\langle \kappa-\kappa_c \rangle}{\Delta\kappa_r}\right)\right] \end{cases} \tag{48}$$

η and $\Delta\kappa_r$ are kinetics related constants. $Y_{DRC} = Y_0$ is considered a constant. $Y_{\max}$ represents the saturation value of the quantity Y_{DRX}.

2.3.2 Mechanisms triggering the MV formation

The micro-voiding triggered during the loading and after unloading are distinguished here.

- During loading

Micro-voids can nucleate during the ductile damage process in several ways. The voids primarily nucleate around inclusions [55] and also at the grain boundary triple points [56] in the material. The void nucleation may be triggered by the particle-matrix interface decohesion, the particle rupture or micro-cracking of the matrix around the particle [57].

- After unloading

As mentioned in section 2.1.1.2, the phase transformation due to quenching of the ASB after unloading provokes the formation of micro-crack at the ASB/matrix interface. The question arises whether the micro-cracks observed by Peirs et al. [1] within the ASB are formed during or after the loading.

The case treated in the current work is effect of MV during the characteristic loading time. In absence of further analytical tools or experimental data, the micro-voiding is tentatively assumed to initiate as soon as the ΔG_{ASB} reaches a transition-to-voiding/critical level ΔG_{ASB}^{crit} such that $G_{MV} = \mathrm{Tr}\left(\mathbf{GN}\right)_{MV} = G_{ASB} + \Delta G_{ASB}^{crit}$. The ΔG_{ASB}^{crit} is calculated as $\Delta G_{ASB}^{crit} = (\Omega - 1) * G_{ASB}$ where Ω is tentatively an arbitrary constant greater than unity. After the MV initiation, ΔG_{ASB} is maintained constant at the value of ΔG_{ASB}^{crit} and ΔG_{MV} evolves taking the predominance as the degradation driving force.

3 NUMERICAL IMPLEMENTATION AND PERFORMANCE EVALUATION

The model in itself does not represent the ASB and MV as entities in the finite elements but it phenomenologically reproduces their consequences in the elements. For a model to be considered predictive, it has to satisfy a complete Verification and Validation (V&V) procedure, (see [20]), which consists in numerically evaluating the performances of the model on initial boundary value problems (IBVP) with increasing complexity against corresponding experimental results. In the literature, the models describing ASB are widely calibrated and evaluated using a single IBVP. Indeed, the high strain rate loading of a hat shaped structure (HSS) is often used to this end, but this should not be considered as a sole evaluating configuration as the ASB orientation and path are entirely controlled by the specimen geometry and the predictability of the model cannot be sufficiently assessed.

In the (V&V) procedure, the model is first numerically implemented at the scale of a representative volume element (RVE) in order to determine the viscoplasticity and

viscous deterioration related constants for a given material from simple experimental results such as those of standard tension/compression tests at various temperatures and strain rates along with high strain rate torsion or/and shear tests. This is the step of material constants **calibration**. The model performance is then evaluated and the constants are further adjusted if needed by considering an initial-boundary value problem (IBVP) for example using a structure, e.g. HSS [4] or Kalthoff and Winkler (KW) impact specimen ([58],[59]), as the ASB path in these structures is known a priori. The set of material constants is expected to satisfy the experimental results obtained from both the simple tests and the tests on the structures. This is the step of **verification**. The final challenging **validation** step is to test the model on a more complex structure where the shear band path is a priori unknown, for example, ballistic impact of a thick plate [4], high speed machining, etc.

In the present work, due to the lack of quantitative experimental results concerning the MV, instead of the V&V, the feasibility and robustness of the enriched model is demonstrated on the RVE and structural scale. The implementation of the model on the complex IBVP namely simulation of high speed machining is a work in progress.

3.1.1 Numerical issues

Dealing numerically with this local softening phenomenon, resulting from a competition between material hardening and softening mechanisms and which has severe irreversible consequences at the structural level, still remains a challenging task. Indeed, the aim is to control the evolution of this material instability all along its progress and accordingly overcome the numerical instability the finite element computation code is subject to in the softening regime and subsequent meshing dependence of the numerical results.

Explicit time integration schemes are considered for both the initial-boundary value problem and rate equations of the constitutive model. In other words, the finite element computation code, namely LS-DYNA, is explicit and the rate equations are integrated within a user material subroutine according to an explicit time integration scheme. The numerical analyses are carried out using brick finite elements (continuum, 3-D, 8-node, reduced integration).

The nonlinear constitutive model implemented as 'user material' subroutine is governed by a system of differential equations which can be written as (see also [60])

$$\dot{F} = A(F,t)F + f(F,t) \;\; ; \;\; F = F\left(v, \rho, \boldsymbol{\tau}, r, \tilde{\mathbf{G}}, \tilde{\mathbf{D}}, T\right) \tag{49}$$

where $A(F,t)$ represents a linear differential operator, and $f(F,t)$ a nonlinear function. The forward finite difference method has been used to integrate the above equations. In the framework of the present study, numerical stability and convergence are furthermore controlled by an adaptive time sub-increment procedure based on the maximum strain increment $\Delta\bar{e}$ principle (see [61]):

$$\overline{\Delta t} = \frac{\Delta\bar{e}}{\dot{\bar{e}}} \; ; \; \dot{\bar{e}} = \sqrt{\frac{2}{3} d_{ij} d_{ji}} \tag{50}$$

where $\overline{\Delta t}$ represents the adaptive time sub-increment, $\dot{\bar{e}}$ a scalar measure of the current strain rate, and $\Delta\bar{e}$ the numerical admissible maximum strain increment. According to (XX), the value of $\overline{\Delta t}$ is dependent on the current strain rate in the element. We are designating Δt_{CFL} the time increment imposed by the explicit computation code LS-DYNA calculated with respect to Courant-Friedrichs-Lewy [62] condition for wave propagation. As long as $\Delta t_{CFL} < \overline{\Delta t}$, the value of $\overline{\Delta t}$ is forced to be equal to the value of Δt_{CFL}, which ensures the numerical stability and convergence from the viewpoint of the numerical integration of the constitutive equations. At high strain rate, the value of $\overline{\Delta t}$ could become lower than the value of Δt_{CFL}. In this case, and for the element concerned, the sampling procedure is activated, using an optimised integration time increment such as $\overline{\Delta t}_{opt} = \frac{\Delta t_{CFL}}{N}$, $N = Int\left(\frac{\Delta t_{CFL}}{\overline{\Delta t}}\right)+1$. The optimised integration time step is determined as follows :

$$\overline{\Delta t}_{opt} = \frac{\Delta t_{CFL}}{N} \quad \text{with} \quad \begin{cases} N = 1 & \text{if} \quad \Delta t_{CFL} \le \overline{\Delta t} \\ N = Int\left(\frac{\Delta t_{CFL}}{\overline{\Delta t}}\right)+1 & \text{if} \quad \Delta t_{CFL} > \overline{\Delta t} \end{cases} \tag{51}$$

This procedure involves a sub loop for the concerned elements only. Considering the great number of elements, this last point is crucial with regards to the calculation and (storage and dynamic) memory costs."

The flow chart describing the different steps of the algorithm is depicted in Fig. 9.

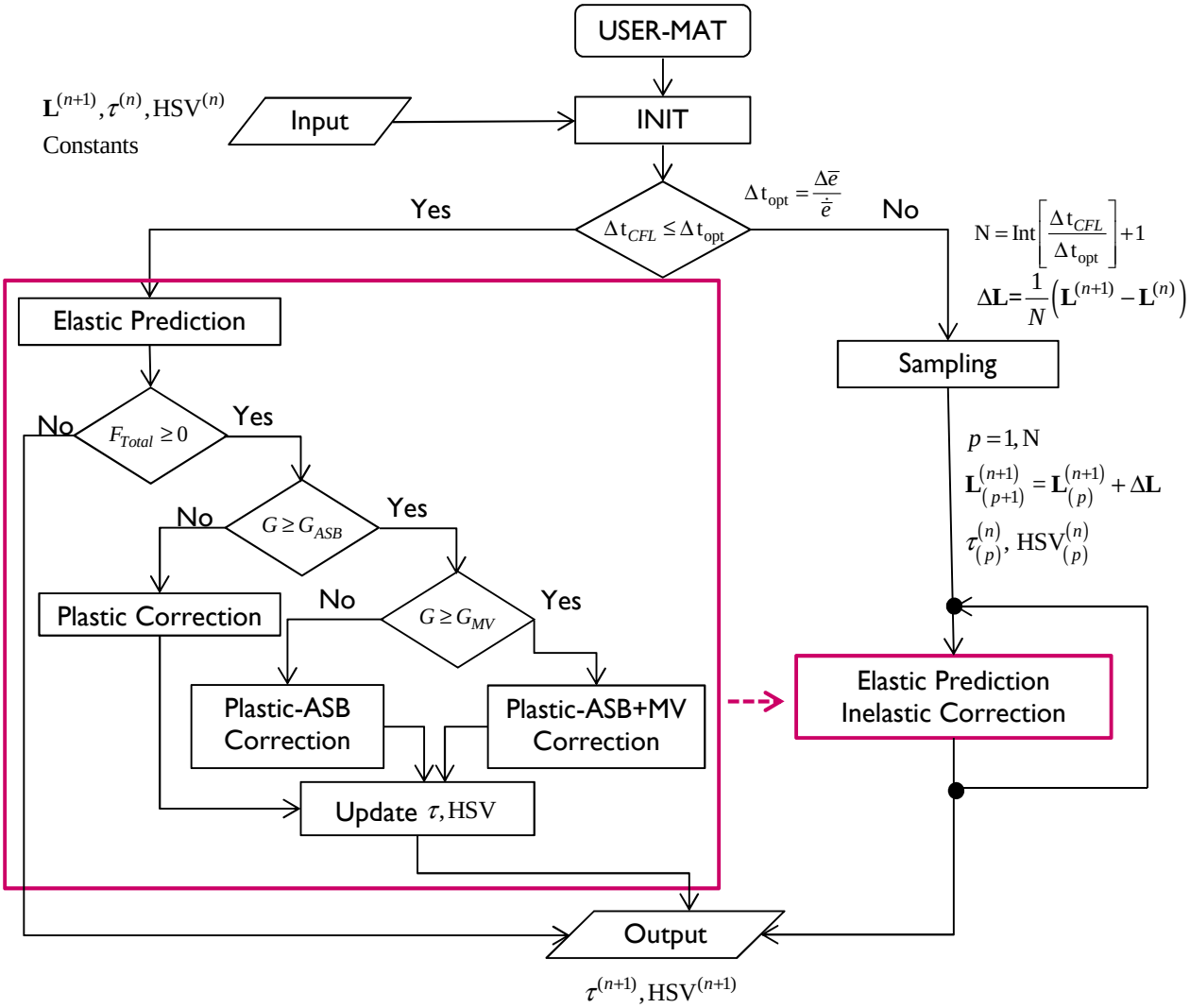

762

763 **Fig. 9** Flow-chart of the algorithm

764 ***3.1.1.1 Regularization and mesh dependence***

765 The viscosity (rate dependency of both plasticity and degradation mechanisms)
766 contributes to regularize the boundary vale problem in the softening regime, see [63],
767 [64]. Yet, as the ASB induces a very strong local softening, additional measures need to
768 be applied to overcome the numerical instability. For this purpose, an adaptive time sub-
769 increment procedure based on maximum strain increment principle (see [61],[29]) is
770 imposed which consists in partitioning the global time increment to obtain a local time
771 increment used to integrate the constitutive equations on the concerned elements.

772 Due to the usage of large scale postulate in the model, an a priori knowledge of the shear
773 band path and hence mesh refining in the selected regions is not required. A study on
774 the influence of the mesh size of the initial model describing the effect of ASB was
775 carried out by Longère et al. [29] and [4]. The large scale postulate requires the ASB to

be embedded within the finite element which in turn implies that it is not feasible to use mesh of any given size. It was shown that a mesh size of approximately five times the shear band (~500μm for high strength steel) width satisfies the scale postulate. A very coarse meshing would give rise to a dispersed area of deteriorated finite elements.

3.1.1.2 Band orientation

According to experimental observations, the ASB is oriented in the plane of the maximum shear stress. This requires the information of the principal stress values. With the knowledge of the plane of maximum shear stress, the resolved shear stress τ_{res} and normal tension stress σ_N are calculated.

3.1.1.3 Stress triaxiality

The ASBs are formed and propagate under conditions of negative or zero stress triaxiality. Accordingly, in the user material subroutine, an external condition is imposed such that the incipience of ASB and the evolution of $\overset{\nabla\ ASB}{\mathbf{D}}$ take place only under positive or nil pressure.

On the other hand, different arguments have been proposed in the literature regarding the stress triaxiality conditions for the formation and growth of micro-voids. Bao and Wierzbicki [65] stated that the micro-voids occur only under positive stress triaxiality and they transform into micro-shear decohesion under an asymptote of -1/3 negative stress triaxiality. However, Longère et al. [27] demonstrated that the micro-voids could initiate and grow around inclusions in the material even under shear pressure loading. The latter view point is adopted herein and hence in the user material subroutine, the MV mechanism is allowed to operate both under negative and positive pressure conditions. The MV expansion is also minimally active in the negative stress triaxiality condition, thanks to its exponential dependence on the mean stress whose form is adopted from Rousselier [33] which itself is derived from Rice and Tracey [38].

3.1.1.4 Crack formation

A material failure criterion is required in order to numerically process the element deletion. A theoretical upper bound for $\mathcal{D}$ from (2) exists considering melting point of the material as the maximum temperature limit which is explained in [21]. The crude theoretical approximation for critical deterioration intensity $\mathcal{D}_c = \mu / b$ is shown in (19).

Numerically implementing the $\mathcal{D}_c$ as a threshold for element failure is not feasible as the elements would undergo excessive distortion (even though LS-DYNA is able to deal with large distortion) at such high values of $\mathcal{D}$. Therefore currently an upper limit for $Tr\mathbf{D}$ is imposed in the user subroutine as a criterion for element deletion. It is to be noted that the numerical simulation of the crack propagation still remains a challenge and it could be dealt with X-FEM in the future, see for example [66], [67], [68], [69].

3.2 NUMERICAL IMPLEMENTATION ON RVE SCALE

The enlarged ASB+MV model is herein numerically implemented on a 3 dimensional RVE i.e. a single brick finite element of *H*-length. The FE is clamped on the bottom and tangentially loaded on the top with a velocity *V* producing simple shearing. The shear strain Γ used in the following is defined as $\Gamma = \int \dot{\Gamma} dt$ where $\dot{\Gamma} = V / H$. Two cases are studying in the following corresponding to two typical materials susceptible to ASB: high strength steel for which the ASB onset is controlled by thermal softening and high strength titanium alloy for which there is a competition between/combination of thermal softening and DRX for the ASB initiation.

3.2.1.1 High strength steel: Thermal softening-controlled ASB onset

The material under consideration is high strength 30 Ni-Cr-Mo 6-6 type steel. The constants pertaining to plasticity and hardening are mostly obtained from [4]. The constants related to the ASB and MV induced softening are assigned arbitrary values in the current performance study.

Table 2 Material properties for 30 Ni-Cr-Mo 6-6 type steel

Elastic - viscoplastic constants:

ρ_0 (kg/m^3)	c_0 (J/kg.K)	E (MPa)	ν	R_∞ (MPa)	R_{int} (MPa)	Y (MPa. s$^{1/n}$)	n
7800	420	200e+3	0.33	400	920	60	6

Thermal properties:

k	υ (°C^{-1})	T_0 (°C)	$\bar{\alpha}$ (/K)	$\dot{\varepsilon}_{crit}$ (/s)
10	1.1e-3	20	1e-6	100

ASB related constants:

Z (MPa. s$^{1/n}$)	m	η_{ASB} (MPa^{-2})	χ_1	χ_2	a (MPa)	b (MPa)
15	2	0.01	0.04	0.04	0	15e+3

MV related constants:

W (MPa. s$^{1/n}$)	q	η_{MV} (MPa^{-2})	ξ	Ω
20	2	0.08	1	1.5

The shear stress – shear strain plot for three different cases of material model are shown in Fig. 10. The response of polycrystalline plasticity material without any localization is shown by the solid blue line. The thermal softening induced slight and smooth drop in strength is seen in this case. The model considering ASB induced deterioration is shown by the red dotted line in which we see a strong drop in strength after ASB onset. The purple dashed line represents the enriched ASB+MV model in which a relatively more abrupt drop in strength is observed due to the additional MV contribution. The drop in stress is attenuated by the viscosity of both ASB and MV. In other words, increasing the velocity, results in a less brutal drop in stress with a smoother slope. The inertial effects which are known to play an important role during void growth, see e.g. [70], are not explicitly accounted for in the present model, but their regularizing consequences are at least partly reproduced thanks to the viscous feature of the MV process. The constants pertaining to the MV in Table 2 are chosen in such a way so as to magnify its effect on the material and kinematics for the sole purpose of visualization.

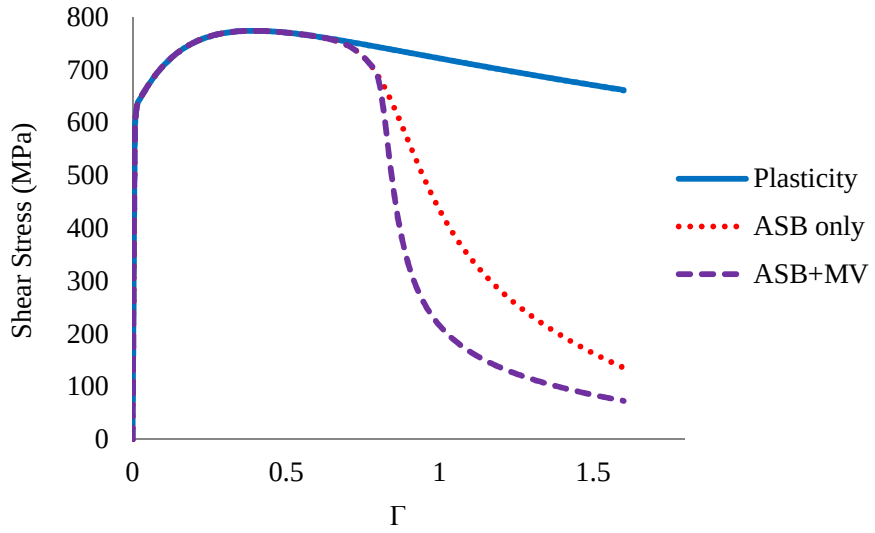

Fig. 10 Shear stress vs Shear strain plots for models with i) polycrystalline plasticity only, ii) plasticity +ASB and iii) plasticity+ ASB+MV

The evolution of the deterioration driving force containing quantities $G = \tilde{\mathbf{G}}:\mathbf{N}$ and ΔG are shown in Fig. 11. Comparing G versus shear strain for ASB and ASB+MV cases, in Fig. 11a, the additional MV induced contribution to G after its onset in the ASB+MV model can be clearly seen. For the ASB+MV model, the progression of ΔG_{ASB} and ΔG_{MV} is plotted in Fig. 11b. After attaining the critical value ΔG_{ASB}^{crit}, ΔG_{ASB} remains constant while ΔG_{MV} initiates and grows. The fact that ΔG_{ASB} is non zero when MV operates allows the ASB-related process to operate until vanishing. In other words, MV becomes progressively and not suddenly predominant, as shown later.

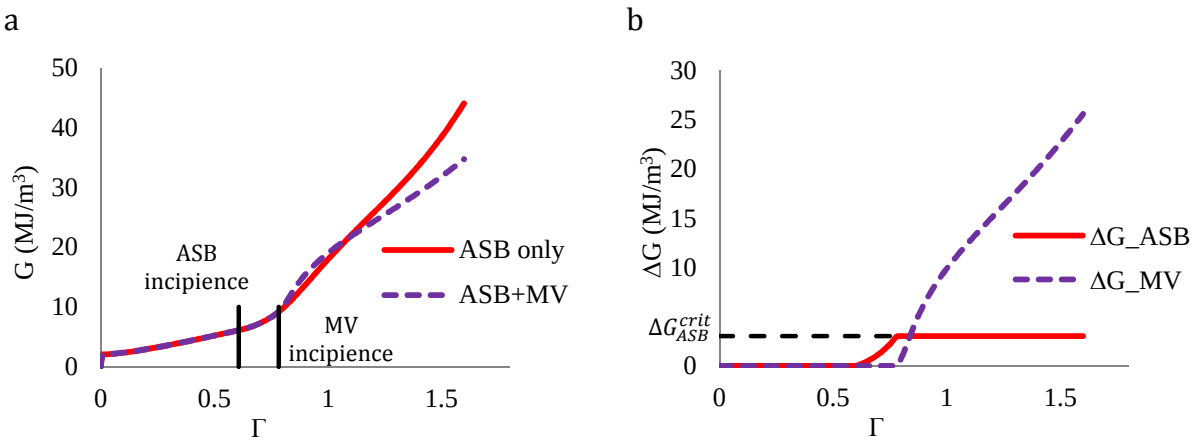

Fig. 11 Deterioration driving force vs. Shear strain (a) **G:N** for models with ASB only and ASB+MV ; (b) ΔG for the ASB+MV model showing the two components

For the ASB+MV model, the total inelastic strain rate d_{12}^{in} and its various components vs the shear strain are shown in Fig. 12. Initially, the d_{12}^{in} is composed of the "regular" polycrystalline plastic strain rate. At the onset of shear localization regular contribution diminishes and the "singular" plastic strain rate becomes progressively predominant. The singular part is composed initially of the ASB induced strain rate $d_{ij}^{in(ASB)}$ and later by the MV induced strain rate $d_{ij}^{in(MV)}$.

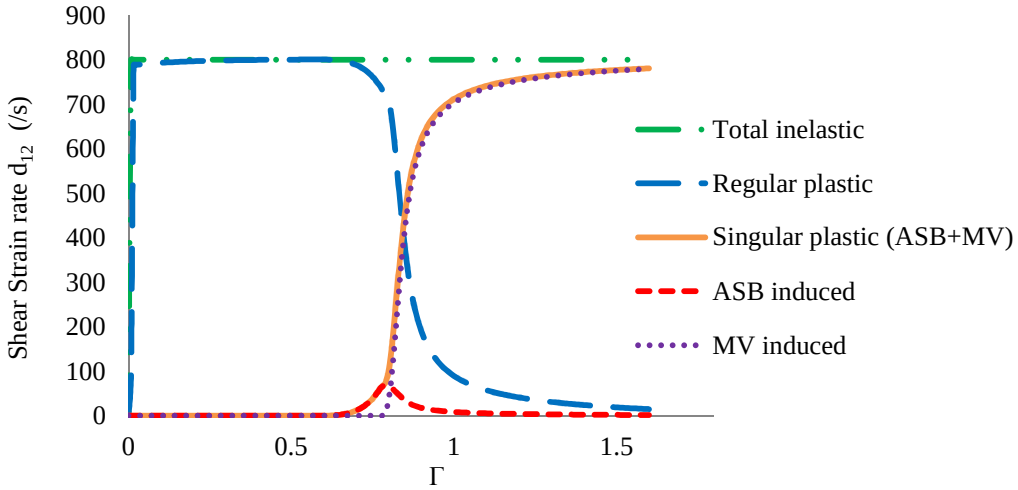

Fig. 12 Inelastic shear strain rate with its components for the ASB+MV model

The evolution of the total deterioration rate $Tr(\overset{\nabla}{\mathbf{D}}^{ASB+MV})$ with its ASB and MV components are presented in Fig. 13a. Finally, Fig. 13b shows the trace of the deterioration tensor for ASB and ASB+MV models. The significant addition to the Tr**D** due to MV is clearly seen.

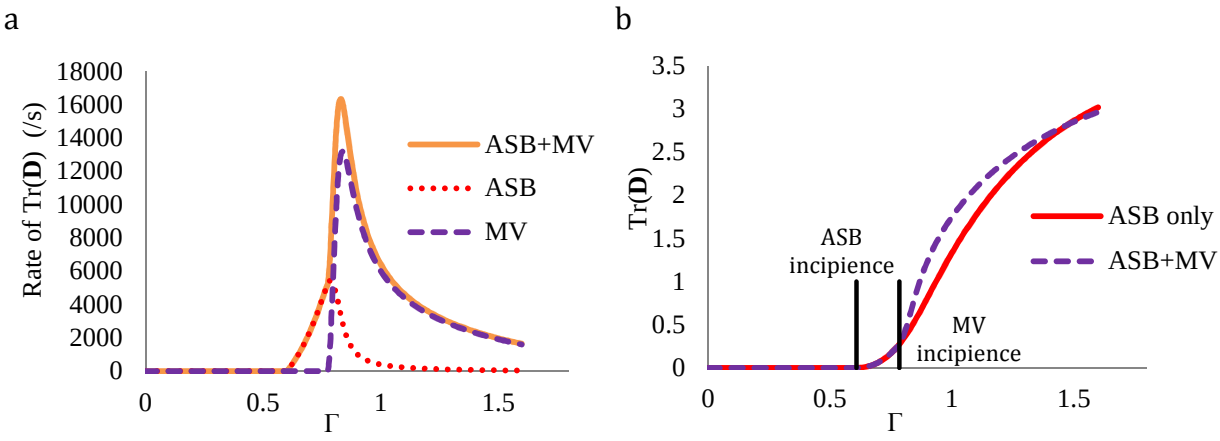

Fig. 13 (a) ASB+MV model: Deterioration rate with its components; (b) Tr**D** for ASB only and ASB+MV models

3.2.1.2 High strength titanium alloy: Influence of dynamic recrystallization

The DRX mechanism is predominantly found to occur in Ti-6Al-4V as a potential cause of softening leading to the formation of ASBs [25]. In this section the enriched ASB+MV constitutive model containing DRX aspects is implemented on the RVE scale i.e. a single brick finite element for the Ti6Al4V alloy. The material properties concerning viscoplasticity and the thermal properties are obtained from experimental results as observed in [30]. The ASB, MV and DRX constants are assigned arbitrary values for the current parametric study.

Table 3 Material properties for Ti-6Al-4V

Elastic - viscoplastic constants:

ρ_0 (kg/m^3)	c_0 (J/kg.K)	E (MPa)	ν	R_∞ (MPa)	R_{int} (MPa)	Y (MPa. s$^{1/n}$)	n
4500	460	113e+3	0.34	972	1080	400	44

Thermal properties:

T_0 (°C)	$\bar{\alpha}$ (/K)	T_{ref} (K)	t	$\dot{\varepsilon}_{crit}$ (/s)
20	1e-6	923	0.6	100

ASB related constants:

Z (MPa. s$^{1/n}$)	m	η_{ASB} (MPa^{-2})	χ_1	χ_2	a (MPa)	b (MPa)
100	2	0.01	0.04	0.04	0	15e+3

MV related constants:

W (MPa. s$^{1/n}$)	q	η_{MV} (MPa^{-2})	ξ	Ω
75	2	0.05	1	2

DRX related constants:

Y_0	Y_{max}	κ_c	$\Delta\kappa_r$	η (MPa)
14	14	0.2	0.8	1.36e+4

In line of the work by [30] dealing with ASB only, the competitive influence of the two softening mechanisms provoking the formation of the ASB, namely thermal softening and DRX induced softening, and their effects on MV are studied here. Four different cases are numerically studied here :

(1) no thermal softening and no DRX (No TS & No DRX)
(2) no thermal softening and with DRX (No TS & With DRX)
(3) with thermal softening and no DRX (With TS & No DRX)
(4) with thermal softening and with DRX (With TS & With DRX)

The DRX related constants are chosen such that the ASB incipience and consequently the start of the drop in strength take place almost at the same time for cases (2) and (3). Fig. 14 shows the plot of shear stress vs shear strain for the four different cases. For the first case, when no softening mechanism comes into play, no material degradation takes place as expected. The ASB incipience instant is marked by a red spot and MV incipience by a green one on the curves. It is seen that as calibrated, the ASB incipience takes place more or less simultaneously for cases (2) and (3) i.e. cases incorporating thermal softening only or DRX softening only. When both the softening mechanisms act in case (4), it is seen that the ASB onset takes place much earlier. The MV onset on the other hand is not directly influenced by the softening mechanisms but it depends on the value of G_{ASB} according to the current model.

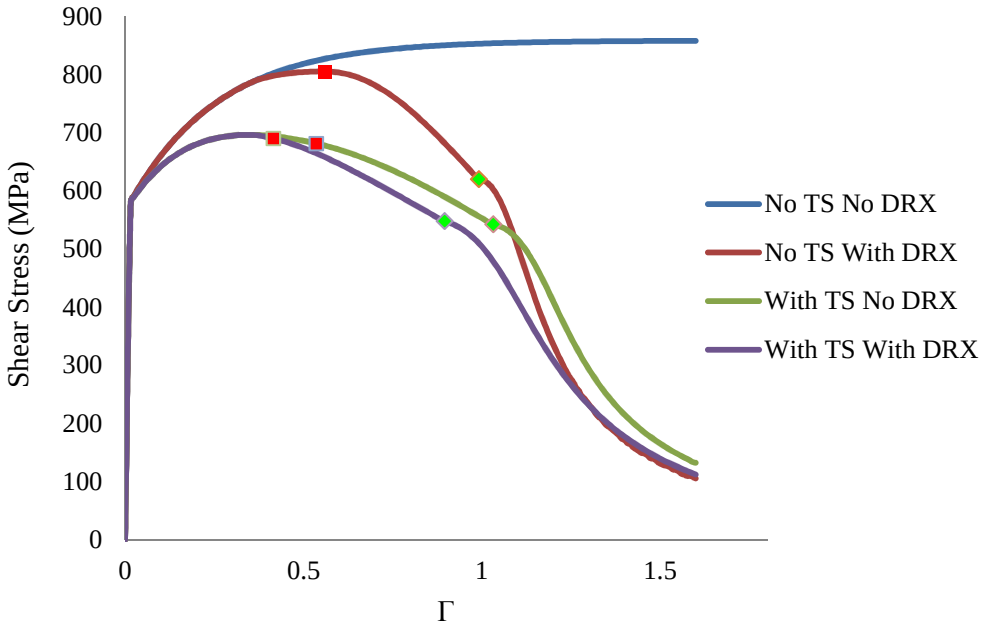

Fig. 14 Shear stress vs shear strain for different cases of thermal softening and DRX induced softning.

3.3 APPLICATION TO INITIAL BOUNDARY VALUE PROBLEMS

Following the V&V principle, the feasibility of the enriched ASB+MV model on an IBVP is demonstrated by simulating the dynamic shearing of a hat shaped structure (HSS). A Couque type HSS [71] (see Fig. 15a) is used to this end. When the HSS is impacted, the inclined gauge section permits constant positive pressure and shear loading creating negative stress triaxiality conditions and thereby making it conducive for ASBs to form. Thus the ASB trajectory (i.e. gauge section) is known a priori and the HSS is suitable for verification of the model. Simulations are carried out for impact of HSS in a direct Hopkinson bar setup made up of tungsten, with a striker bar velocity of 30 m/s; see Fig. 15.

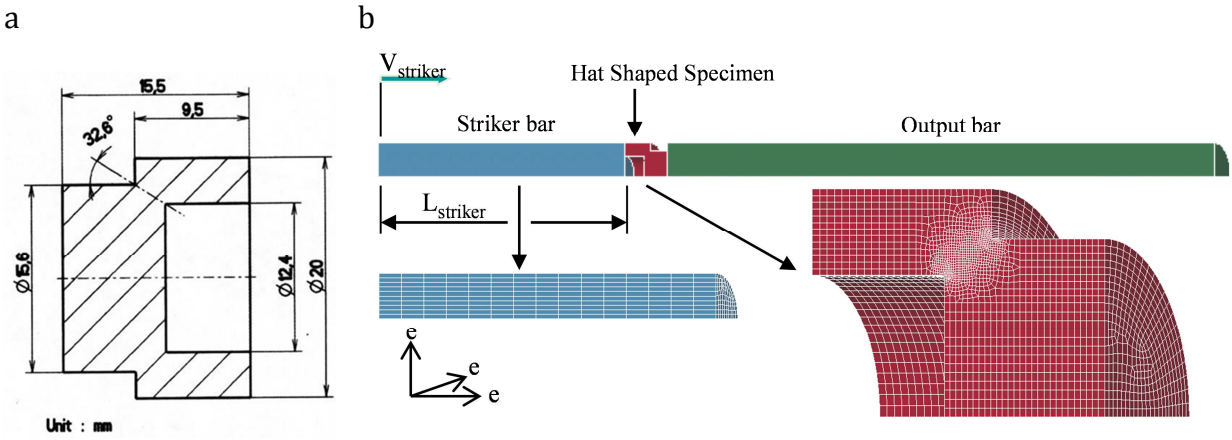

Fig. 15 (a) Hat Shaped Structure; (b) Direct Hopkinson bar setup. After Longère et al. [4].

3.3.1 Case of High Strength Steel

As it is the case of steel, only thermal softening is taken into account as the softening mechanism leading to the formation of ASB. The ASB and MV related material constants used here for 30 Ni-Cr-Mo 6-6 steel are shown in Table 2. As in the elementary responses of the RVE examined in section 3.2, two configurations are studied in the following: (i) configuration describing ASB effect only, i.e. with MV onset being deactivated, and (ii) configuration reproducing both ASB and MV effects where ASB-related constants are the same as those used in (i).

Firstly, the resolved shear stress τ_{res} is examined as function of time for the elements in the gauge section, as shown in **Fig. 16**, of the HSS. The ASB model shows a relatively mild drop in strength in Fig. 17a after the ASB onset whereas the loss of strength is accelerated by the presence of MV in Fig. 17 for the ASB+MV model.

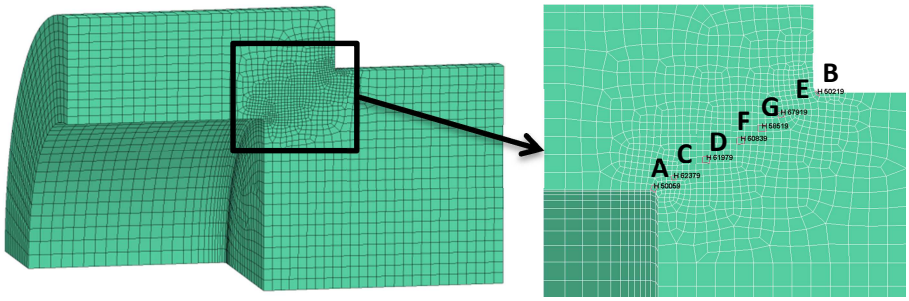

Fig. 16 Finite elements in the gauge section selected for plots.

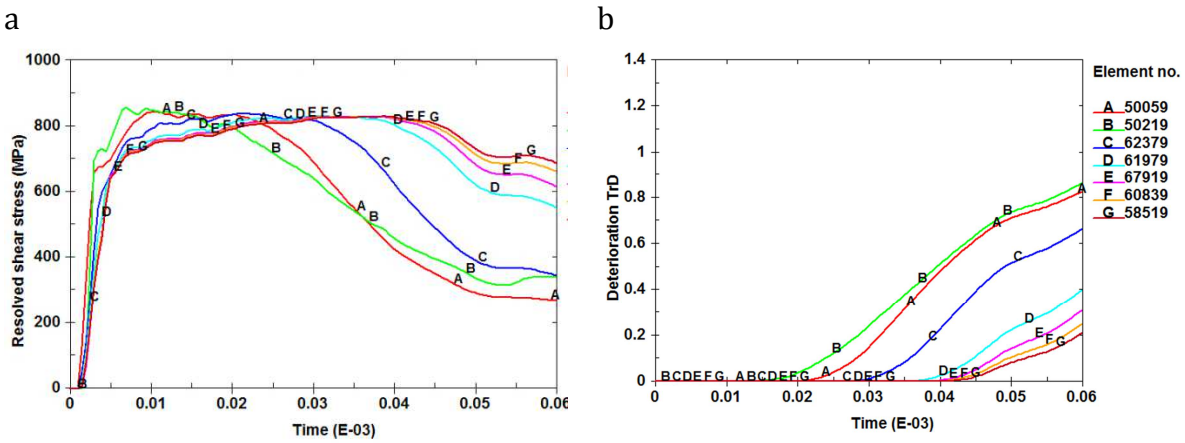

Fig. 17 Numerical simulation of the dynamic loading of hat shaped structure. Model: ASB only. a) Resolved shear stress history. b) Deterioration variable history. See **Fig. 16**. for the location of the elements.

The evolution of the deterioration variable $Tr\mathbf{D}$ for ASB and ASB+MV is plotted in Fig. 18,18b. As expected, the deterioration intensity is significantly higher for the ASB+MV case when compared with the ASB only model.

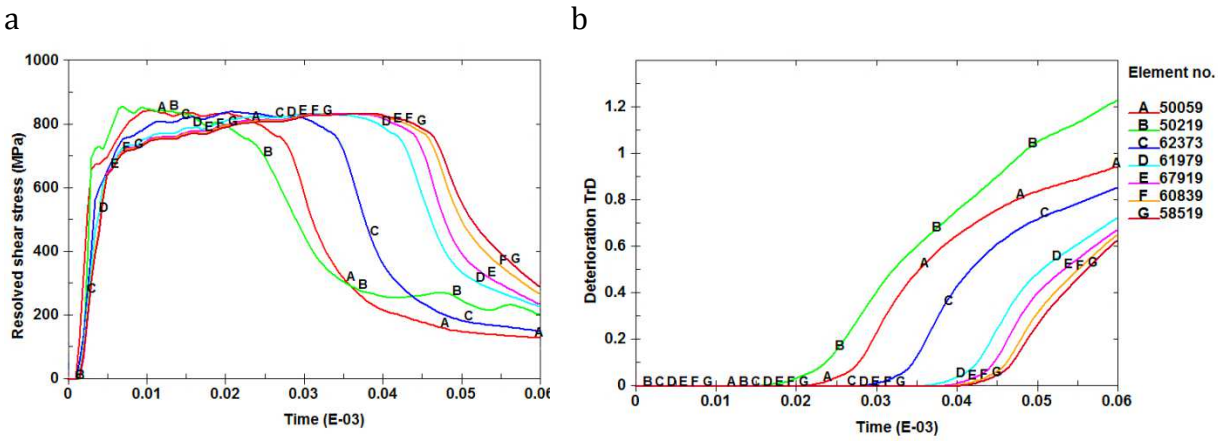

Fig. 18 Numerical simulation of the dynamic loading of hat shaped structure. Model: ASB +MV. a) Resolved shear stress history. b) Deterioration variable history. See **Fig. 16**. for the location of the elements.

The numerical deterioration maps shown in the following give an indication of the presence of ASB/MV in the finite elements. In Fig. 19, for the model considering ASB only, the elements in red contain ASB. Likewise for the ASB+MV model in Fig. 20, the elements with ASB are highlighted in red (Fig. 20a) and the ones containing MV in blue (Fig. 20b).

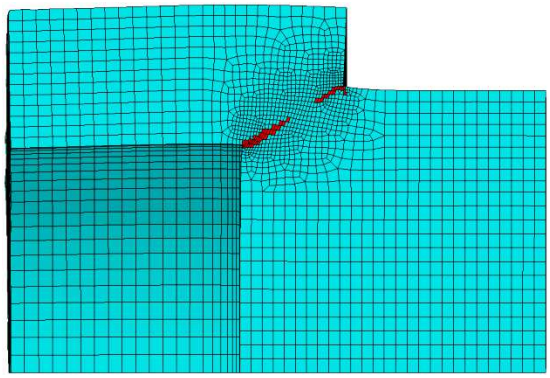

Fig. 19 Model with ASB only: Deterioration indicator at 39μs. Elements in red are subjected to ASB.

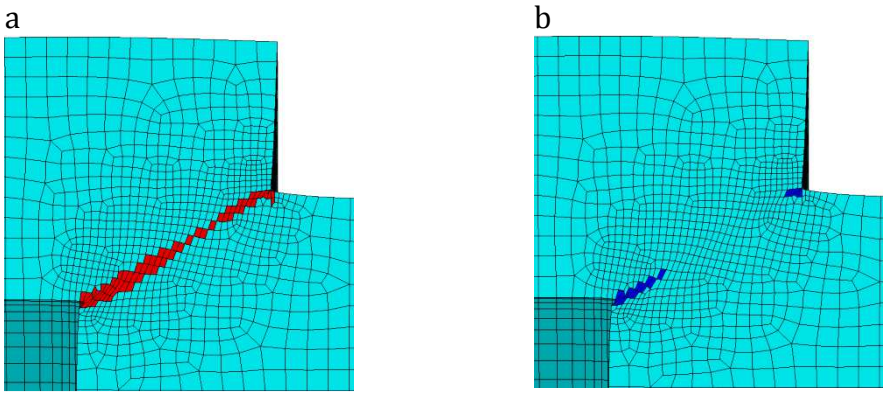

Fig. 20 Model with ASB+MV: Deterioration indicator at 39μs. a) Elements in red are subjected to ASB. b) Elements in blue are subjected to MV.

These numerical results bring two comments. Firstly, at the same time, considering ASB only leads to a partial propagation of ASB in the gauge section (Fig. 19), whereas considering both ASB+MV leads to a complete propagation of ASB (Fig. 20). MV in ASB wake thus contributes in propagating the ASB farther. Secondly, according to Fig. 20 and assuming that the loading ends at the time considered, although ASB has propagated throughout the whole structure, MV zones cover very limited areas, viz. near the specimen corners. . The material in the ligament between the MV zones, which has been subject to ASB, may recover its initial properties after unloading due to phase transformation. In other words, the remaining effect of ASB+MV may reduce to MV alone with only local parts of the structure affected. In another scenario, the quenching of the material of ASB after unloading and cooling may cause micro-cracking, leading to a complete fracture of the structure.

3.3.2 Case of Ti6Al4V

As mentioned in Section 2.3.1.2, the works of Rittel and co-workers [25] suggest that, for materials such as high strength Ti alloys, the phenomenon of dynamic recrystallization (DRX) potentially needs to be taken into account in ASB initiation. Unlike the common assumption that DRX is a consequence of ASB, they argue that the DRX not only precedes the ASB but is also a dominant microstrutural factor in the very generation of the band. Osovski et al. [45] concluded that the respective influence of thermal and DRX induced softening depends on the chronology of the process and the material considered: in case of Ti6Al4V, DRX develops earlier and overrides the thermal softening effects; on the other extreme case of pure titanium which does not undergo DRX, the thermal softening plays a dominant role in the ASB initiation. In the line of their work, the competition occurring between thermal and DRX induced softening is analyzed here on a structural scale. The materials constants of Ti6Al4V are shown in Table 3.

In order to study the potential effect of DRX on ASB formation and evolution, two cases are examined in the simulation of HSS:
(1) no thermal softening and with DRX (No TS & With DRX)
(2) with thermal softening and with DRX (With TS & With DRX)
These configurations have to be considered together with those studied in Section 3.2.1.2.

The resolved shear stresses for both cases for the selected elements in the gauge section (as shown in Fig. 16) of the HSS are plotted in Fig. 21a,b. In the graphs, the red marks indicate the ASB onset and the green ones MV onset. While examining the two cases for the instant of ASB onset, it is clearly seen that the case with combined DRX and thermal softening (Fig. 21b) shows relatively early onset of ASB when compared to the case of DRX induced softening only (Fig. 21a). Consequently the MV onset also takes place earlier for the former case than the latter. The results seen here is similar to the ones observed in the corresponding cases for the single FE in Chapter 2, Section 2.5.2.2.

The deterioration maps showing the elements with ASB and MV activated respectively at a given instant (viz. 45μs) for the above two cases are shown in Fig. 22. In the case considering DRX induced softening solely (Fig. 22a), fewer elements show ASB and MV at the given instant. The combined influence of thermal and DRX induced softening seems to have accelerated the ASB and MV onset which is seen in the deterioration map (Fig. 22b) in which relatively more elements are seen with the presence of ASB and MV.

As a consequence, neglecting the thermal softening and considering only DRX induced softening for materials such as Ti6Al4V as proposed by Osovski et al. [45], would lead to delay of ASB initiation and underestimation of the ASB propagation. However more

experimental evidence is needed to characterize each material in terms of the respective influence of thermal and DRX induced softening on the shear localization onset.

a

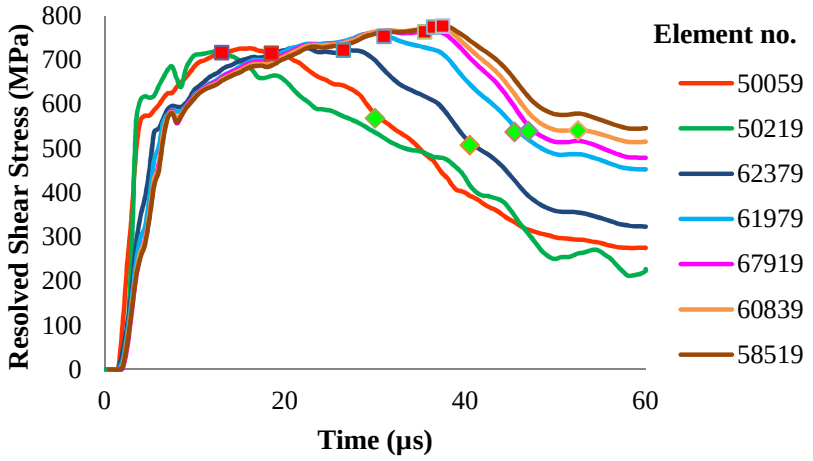

b

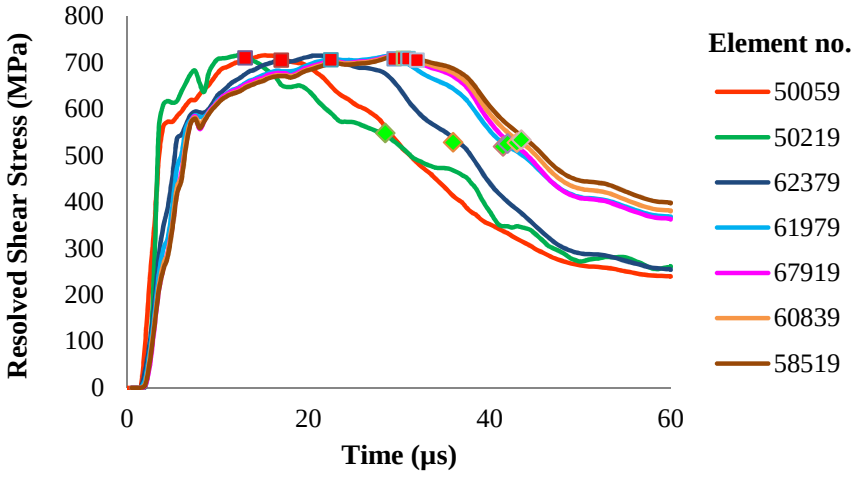

Fig. 21 Model ASB+MV: Deterioration variable history of elements in the gauge section, see **Fig. 16**. a) Case of no thermal softening and with DRX b) Case considering thermal softening and DRX.

3.3.3 Experimental vs. numerical results confrontation

In order to assess the prediction ability of the model to describe ASB and further micro-voiding, numerical results are compared with experimental ones. Material constants are reported in Table 4. Two configurations extracted from [4] are considered in the present work:

- moderate impact configuration with $L_{striker}$=90mm and $V_{striker}$=23.7m/s, see Fig. 23, leading to incomplete ASB and MV propagation, see macrograph,
- severe impact configuration with $L_{striker}$=90mm and $V_{striker}$=23.7m/s, see Fig. 24, leading to complete ASB and MV propagation, see macrograph.

In the moderate impact configuration, see Fig. 23 left, ASBs are shown to form from the specimen corners and propagate partially. A small crack has formed in the ASBs wake. In Fig. 23 right related to the numerical simulation, the same trend is observed where the damaged area length is slightly smaller than the ASB length. In the severe impact configuration, see Fig. 24 left, ASBs initiated from the corners join together to form a single band as do the cracks, leading to the complete fracture of the specimen. The same trend is observed once again in the numerical simulations. The comparison of the experimental macrograph, on the left, with the ASB and MV indicator maps, on the right, and of the history of the experimental and numerical axial stress on the left allows for concluding to a fair agreement.

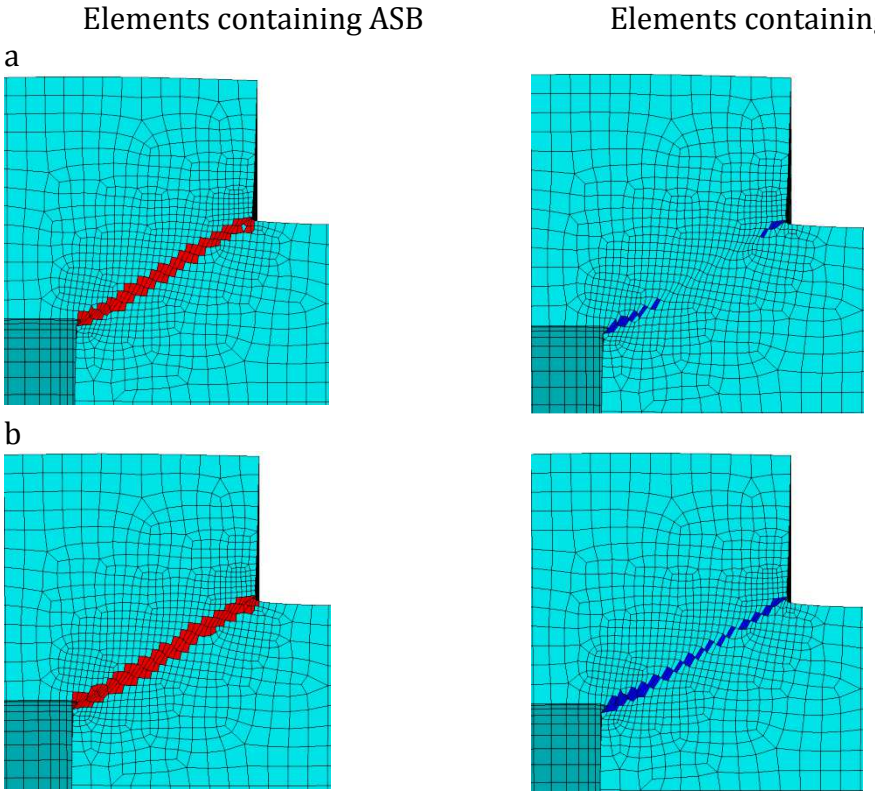

Fig. 22 Model with ASB+MV: Deterioration indicator at 45μs. Elements in red are subjected to ASB. Elements in blue are subjected to MV. a) Case of no thermal softening and with DRX b) Case considering thermal softening and DRX.

3.3.4 Discussion/assessment

The realistic description of initiation and propagation of ASB and MV and their consequences on the structural material in a wide range of situations implies modelling as close as possible to the complex physics of the mechanisms while being tractable and applicable to initial boundary value problems. The enriched ASB+MV three-dimensional constitutive model is herein demonstrated to be feasible on a structural scale and shows the desired qualitative performance on the IBVP.

Table 4 Material properties for 30 Ni-Cr-Mo 6-6 steel

Elastic - viscoplastic constants:

ρ_0 (kg/m^3)	c_0 (J/kg.K)	E (MPa)	ν	R_∞ (MPa)	R_{int} (MPa)	Y (MPa. s$^{1/n}$)	n
7800	420	200e+3	0.33	400	920	60	6

Thermal properties:

k	υ (°C^{-1})	T_0 (°C)	$\bar{\alpha}$ (/K)	$\dot{\varepsilon}_{crit}$ (/s)
10	1.1e-3	20	1e-6	100

ASB related constants:

Z (MPa. s$^{1/n}$)	m	η_{ASB} (MPa^{-2})	χ_1	χ_2	a (MPa)	b (MPa)
19	2	0.12	0.05	0.05	0	15e+3

MV related constants:

W (MPa. s$^{1/n}$)	q	η_{MV} (MPa^{-2})	ξ	Ω
20	2	0.08	1	1.5

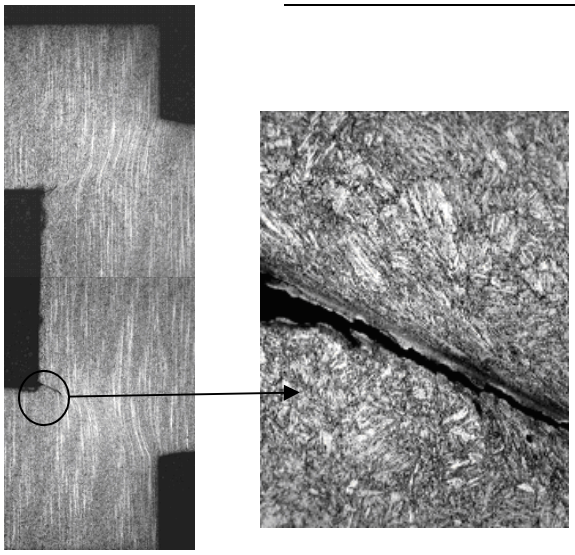

Macrograph

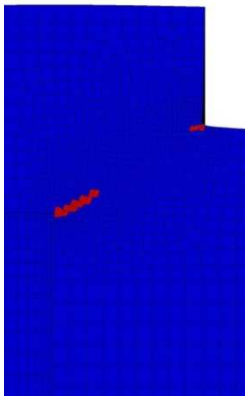

ASB indicator map

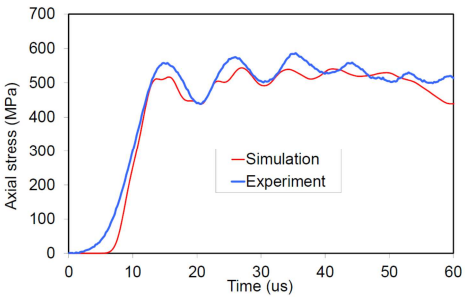

Axial stress transmitted into the output bar

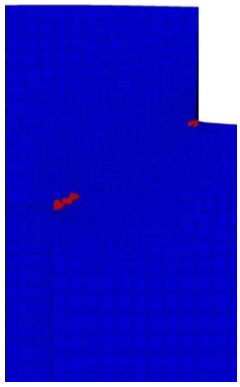

MV indicator map

Fig. 23 Configuration with $L_{striker}$=90mm ; $V_{striker}$=23.7m/s. Incomplete ASB and MV propagation. left: Post-mortem macrograph and Axial experimental and numerical stress transmitted into the output bar ; right: Numerical deterioration map (100 µs).

- ASB only vs. ASB+MV

While comparing the two models exhibiting ASB only and ASB+MV when implemented on a structural scale, the following conclusion can be drawn. The model with ASB and MV activated exhibits increased deterioration intensity and therefore accelerates the drop in strength of the material which is the expected behaviour. Also, while comparing with the ASB only model, the presence of MV advances the ASB propagation.

Not all elements containing ASB show the presence of MV at a given instant. This would imply that, upon loading at that given instant, if the material within the ASB recovers its initial properties due to phase transformation, the only deteriorated region would be the elements containing MV. It is thus essential to distinguish the two mechanisms of ASB and MV.

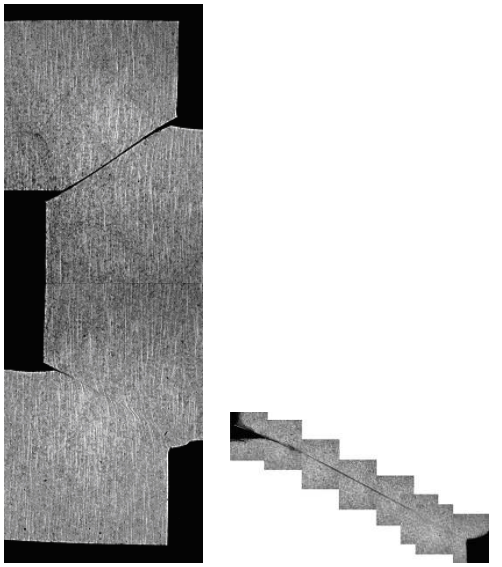

Macrograph

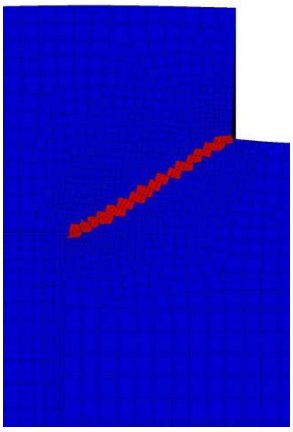

ASB indicator map

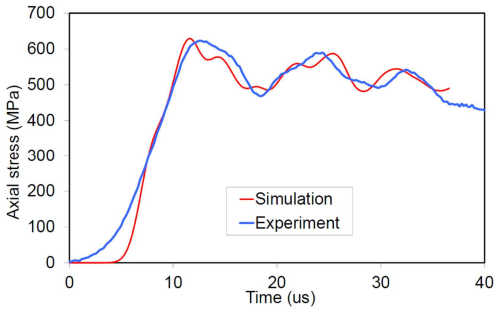

Axial stress transmitted into the output bar

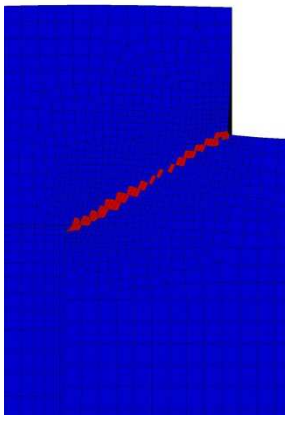

MV indicator map

Fig. 24 : Configuration with Lstriker=40mm ; Vstriker=35.6m/s. Complete ASB and MV propagation. left: Post-mortem macrograph and Axial experimental and numerical stress transmitted into the output bar ; right: Numerical deterioration map (40 µs)

- DRX vs. DRX+TS

In case of materials susceptible to DRX such as high strength Ti alloys, in addition to thermal softening, the DRX induced softening plays a role on the ASB onset. The influence of the two softening mechanisms has been studied here concerning two cases namely DRX only and DRX+TS. It is seen that the combined DRX+TS leads to a much earlier onset of ASB and consequently MV when compared to the case with DRX induced softening only. It is therefore important to consider both the softening mechanisms in order to be conservative in the engineering approach.

4 CONCLUSION

A physics motivated phenomenological model describing ASB and MV effects developed in a large scale postulate has been applied herein in accordance with the physics of the shear localization and subsequent ductile damage process. The two main effects of ASB+MV induced deterioration reproduced by the unified model are: material consequence, viz. anisotropic deterioration of the material elastic and plastic properties; and kinematic consequence, viz. progressive deviation of the plastic flow in the band plane and then according to the micro-void orientation. The present enlarged ASB+MV model is numerically implemented as user material in the engineering finite element computation code LS-DYNA. The model has been successfully demonstrated to be numerically feasible at the representative volume element scale and also on a structure namely the hat shaped structure (HSS). The ASB+MV model distinguishes the ASB and MV induced effects in the late pre-failure stage and the supplementary MV contribution to the deterioration could be observed.

The qualitative analysis of the ASB+MV model is done by comparing with ASB only model in which the MV is deactivated while maintaining the ASB related constants. On the scale of the RVE, the ASB+MV model demonstrates the desired behaviour by showing supplementary MV induced material deterioration and kinematics. On the HSS, it is observed that the presence of MV accelerates the propagation of ASB which has not been shown in literature and thus constitutes a novel result. Also, at a given instant, not all elements containing the ASB reach the criteria for MV onset; only the corner elements show the presence of MV. One could infer the following possible scenarios from the given state of elements on unloading: the material within the ASB might recover its initial properties after being quenched by the surrounding material and thus phase transformed leaving only the effect of MV in the respective elements in the corners; or the cooling on unloading might cause micro-cracking within the ASB leading to complete fracture. The respective influence of thermal and dynamic recrystallization (DRX) induced softening is also studied on the RVE and structural scale. In both the cases it is shown that the combined contribution of thermal and DRX softening brings about an earlier ASB onset as expected. Considering only one of the softening mechanisms would

delay the ASB onset and underestimate the ASB propagation, which is in contradiction with some assumptions in literature considering that DRX is the unique mechanism controlling the ASB onset particularly in Ti-6Al-4V titanium alloy.

The challenge still remains in terms of identifying the instant of MV incipience from experiments and hence to distinguish ASB and MV related material constants. Also, in order to account for the different orientation of the MV with respect to ASB, experimental observations are required.

REFERENCES

[1] J. Peirs, P. Verleysen, J. Degrieck, and F. Coghe, "The use of hat-shaped specimens to study the high strain rate shear behaviour of Ti – 6Al – 4V," *Int. J. Impact Eng.*, vol. 37, no. 6, pp. 703–714, 2010.

[2] Q. Xue, M. A. Meyers, and V. F. Nesterenko, "Self-organization of shear bands in titanium and Ti-6Al-4V alloy," *Acta Mater.*, vol. 50, no. 3, pp. 575–596, 2002.

[3] D.-G. Lee, Y. H. Lee, S. Lee, C. S. Lee, and S.-M. Hur, "Dynamic deformation behavior and ballistic impact properties of Ti6Al4V alloy having equiaxed and bimodal microstructures," *Met. Mater. Trans. A*, vol. 35 A, no. October, pp. 3103–3112, 2004.

[4] P. Longère, A. Dragon, and X. Deprince, "Numerical Study of Impact Penetration Shearing Employing Finite Strain Viscoplasticity Model Incorporating Adiabatic Shear Banding," *ASME, J. Eng. Mater. Technol.*, vol. 131, no. 1, pp. 011105.1–011105.14, 2009.

[5] B. E. Schuster, J. P. Ligda, Z. L. Pan, and Q. Wei, "Nanocrystalline refractory metals for extreme condition applications," *JOM*, vol. 63, no. 12, pp. 27–31, 2011.

[6] W. S. Andrews, "Depleted Uranium on the battlefield," *Can. Mil. J.*, pp. 41–46, 2003.

[7] L. S. Magness Jr., "High strain rate deformation behaviors of kinetic energy penetrator materials during ballistic impact," *Mech. Mater.*, vol. 17, pp. 147–156, 1994.

[8] A. Molinari, C. Musquar, and G. Sutter, "Adiabatic shear banding in high speed machining of Ti – 6Al – 4V : experiments and modeling," *Int. J. Plast.*, vol. 18, pp. 443–459, 2002.

[9] G. G. Ye, S. F. Xue, M. Q. Jiang, X. H. Tong, and L. H. Dai, "Modeling periodic adiabatic shear band evolution during high speed machining Ti-6Al-4V alloy," *Int. J. Plast.*, vol. 40, pp. 39–55, 2013.

[10] C. McVeigh, F. Vernerey, W. K. Liu, B. Moran, and G. Olson, "An interactive micro-void shear localization mechanism in high strength steels," *J. Mech. Phys. Solids*, vol. 55, no. 2, pp. 225–244, 2007.

[11] A. G. Odeshi, S. Al-ameeri, S. Mirfakhraei, F. Yazdani, and M. N. Bassim, "Deformation and failure mechanism in AISI 4340 steel under ballistic impact," *Theor. Appl. Fract. Mech.*, vol. 45, pp. 18–24, 2006.

[12] H. C. Rogers and C. V. Shastry, "Material Factors in Adiabatic Shearing in Steels," in *Shock Waves and High-Strain -Rate Phenomena in Metals - Concepts and Applications*, Plenum Pre., M. A. Meyers and L. E. Murr, Eds. 1981, pp. 285–298.

[13] J. Peirs, W. Tirry, B. Amin-Ahmadi, F. Coghe, P. Verleysen, L. Rabet, D. Schryvers, and J. Degrieck, "Microstructure of adiabatic shear bands in Ti6Al4V," *Materials Characterization*, vol. 75. 2013.

[14] A. Bonnet-Lebouvier, A. Molinari, and P. Lipinski, "Analysis of the dynamic propagation of adiabatic shear bands," *Int. J. Solids Struct.*, vol. 39, no. 16, pp. 4249–4269, 2002.

[15] X. Teng, T. Wierzbicki, and H. Couque, "On the transition from adiabatic shear banding to fracture," *Mech. Mater.*, vol. 39, no. 2, pp. 107–125, 2007.

[16] S. Su, L. Stainier, and S. Mercier, "Eergy-based variational modeling of fully formed adiabatic shear

bands," *Eur. J. Mech. / A Solids*, vol. 47, pp. 1–13, 2014.

[17] P. M. A. Areias and T. Belytschko, "Two-scale method for shear bands: Thermal effects and variable bandwidth," *Int. J. Numer. Methods Eng.*, vol. 72, pp. 658–696, 2007.

[18] H. M. Mourad, C. A. Bronkhorst, V. Livescu, J. N. Plohr, and E. K. Cerreta, "Modeling and simulation framework for dynamic strain localization in elasto-viscoplastic metallic materials subject to large deformations," *Int. J. Plast.*, vol. 88, pp. 1–26, 2017.

[19] A. Tabarraei, J.-H. Song, and H. Waisman, "A two-scale strong discontinuity approach for evolution of shear bands under impact loads," *Int. J. Multiscale Comput. Eng.*, vol. 11, pp. 543–563, 2013.

[20] P. Longère, "Adiabatic shear banding assisted dynamic failure: Some modeling issues," *Mech. Mater.*, vol. 116, pp. 49–66, 2018.

[21] P. Longère, A. Dragon, H. Trumel, T. De Resseguier, X. Deprince, and E. Petitpas, "Modelling adiabatic shear banding via damage mechanics approach," *Arch. Mech.*, vol. 55, no. 1, pp. 3–38, 2003.

[22] P. Longere and A. Dragon, "Enlarged finite strain modelling incorporating adiabatic shear banding and post-localization microvoiding as shear failure mechanisms," *Int. J. Damage Mech.*, pp. 1–28, 2016.

[23] A. Marchand and J. Duffy, "An experimental study of the formation process of adiabatic shear bands in a structural steel," *J. Mech. Phys. Solids*, vol. 36, no. 3, pp. 251–283, 1988.

[24] C. Zener and J. H. Hollomon, "Effect of Strain Rate Upon Plastic Flow of Steel," *J. Appl. Phys.*, no. 15, pp. 22–32, 1944.

[25] D. Rittel, P. Landau, and A. Venkert, "Dynamic Recrystallization as a potential cause for adiabatic shear failure," *Phys. Rev. Lett.*, vol. 101, no. 165501, 2008.

[26] P. Landau, S. Osovski, A. Venkert, V. Gärtnerová, and D. Rittel, "The genesis of adiabatic shear bands," *Nature, Sci. Reports*, vol. 6: 37266, 2016.

[27] P. Longère, S. Bhogaraju, and D. Craciun, "Void collapse/growth in solid materials under overall shear loading," *Mech. Res. Commun.*, vol. 69, pp. 1–7, 2015.

[28] X. Liu, C. Tan, J. Zhang, Y. Hu, H. Ma, F. Wang, and H. Cai, "Influence of microstructure and strain rate on adiabatic shearing behavior in Ti-6Al-4V alloys," *Mater. Sci. Eng. A*, vol. 501, no. 1–2, pp. 30–36, 2009.

[29] P. Longère, A. Dragon, H. Trumel, and X. Deprince, "Adiabatic shear banding-induced degradation in a thermo-elastic / viscoplastic material under dynamic loading," *Int. J. Impact Eng.*, vol. 32, pp. 285–320, 2005.

[30] P. Longère, "Respective/combined roles of thermal softening and dynamic recrystallization in adiabatic shear banding initiation," *Mech. Mater.*, vol. 117, pp. 81–90, 2018.

[31] D. Halm and A. Dragon, "A Model of Anisotropic Damage by Mesocrack Growth; Unilateral Effect," *Int. J. Damage Mech.*, vol. 5, pp. 384–402, 1996.

[32] J. Lemaitre, "A Continuous Damage Mechanics Model for Ductile Fracture," *J. Eng. Mater. Technol.*, vol. 107, pp. 83–89, 1985.

[33] G. Rousselier, "Ductile fracture models and their potential in local approach of fracture," *Nucl. Eng. Des.*, vol. 105, pp. 97–111, 1987.

[34] V. Tvergaard and A. Needleman, "Analysis of the Cup-Cone Fracture in a Round Tensile bar," *Acta Metall.*, vol. 32, no. 1, pp. 157–169, 1984.

[35] R. Becker, A. Needleman, O. Richmond, and V. Tvergaard, "Void Growth and Failure in Notched bars," *J. Mech. Phys. Solids*, vol. 36, no. 3, pp. 317–351, 1988.

[36] H. L. Dorothy, P. Longère, and A. Dragon, "Modelling of high strain rate failure under ASB and microvoiding," *Procedia Eng.*, vol. 173, pp. 593–600, 2017.

[37] H. L. Dorothy, P. Longère, and A. Dragon, "Coupled ASB-and-microvoiding-assisted dynamic ductile failure," *Procedia Eng.*, vol. 197, pp. 60–68, 2017.

[38] J. R. Rice and D. M. Tracey, "On the ductile enlargement of voids in triaxial stress fields," *J. Mech. Phys. Solids*, vol. 17, pp. 201–217, 1969.

[39] M. Zhou, G. Ravichandran, and A. J. Rosakis, "Dynamically Propagating Shear Bands in Impact-Loaded Plates-II. Numerical Simulations," *J. Mech. Phys. Solids*, vol. 44, no. 6, 1996.

[40] M. Dolinski, D. Rittel, and A. Dorogoy, "Modeling adiabatic shear failure from energy considerations," *J. Mech. Phys. Solids*, vol. 58, no. 11, pp. 1759–1775, 2010.

[41] L. Anand, K. H. Kim, and T. G. Shawk, "Onset of shear localization in viscoplastic solids," *J. Mech. Phys. Solids*, vol. 35, no. 4, pp. 407–429, 1987.

[42] A. Molinari, "Instabilité thermoviscoplastique en cisaillement simple," *J. mécanique théorique appliquée*, vol. 4, no. 5, pp. 659–684, 1985.

[43] P. Longère and A. Dragon, "Adiabatic Heat Evaluation For Dynamic Plastic Localization," *J. Theor. Appl. Mech.*, vol. 45, no. 2, pp. 203–223, 2007.

[44] P. Longère, "Some issues related to the modeling of dynamic shear localization- assisted failure," in *Dynamic Damage and Fragmentation*, O. Cazacu and E. Buzuard, Eds. ISTE-WILEY, to be published.

[45] S. Osovski, D. Rittel, and A. Venkert, "The respective influence of microstructural and thermal softening on adiabatic shear localization," *Mech. Mater.*, vol. 56, pp. 11–22, 2013.

[46] A. Needleman and V. Tvergaard, "Analysis of a brittle-ductile transition under dynamic shear loading," *Int. J. Solids Struct.*, vol. 32, no. 17–18, pp. 2571–2590, 1995.

[47] J. J. Mason, A. J. Rosakis, and G. Ravichandran, "On the strain and strain rate dependence of the fraction of plastic work converted to heat: an experimental study using high speed infrared detectors and the Kolsky bar," *Mech. Mater.*, vol. 17, no. 2–3, pp. 135–145, 1994.

[48] P. Longère and A. Dragon, "Evaluation of the inelastic heat fraction in the context of microstructure-supported dynamic plasticity modelling," *Int. J. Impact Eng.*, vol. 35, no. 9, pp. 992–999, 2008.

[49] P. Longère and A. Dragon, "Inelastic heat fraction evaluation for engineering problems involving dynamic plastic localization phenomena," *J. Mech. Mater. Struct.*, vol. 4, no. 2, pp. 319–349, 2009.

[50] L. Stainier and M. Ortiz, "Study and validation of a variational theory of thermo-mechanical coupling in finite visco-plasticity," *Int. J. Solids Struct.*, vol. 47, no. 5, pp. 705–715, 2010.

[51] M. Meyers, V. Nesterenko, J. LaSalvia, and Q. Xue, "Shear localization in dynamic deformation of materials: microstructural evolution and self-organization," *Mater. Sci. Eng. A*, vol. 317, no. 1, pp. 204–225, 2001.

[52] G. A. Li, L. Zhen, C. Lin, R. S. Gao, X. Tan, and C. Y. Xu, "Deformation localization and recrystallization in TC4 alloy under impact condition," *Mater. Sci. Eng. A*, vol. 395, pp. 98–101, 2005.

[53] B. Wang, J. Li, J. Sun, X. Wang, and Z. Liu, "Shear localization and its related microstructural evolution in the ultrafine grained titanium processed by multi-axial compression," *Mater. Sci. Eng. A*, vol. 612, pp. 227–235, 2014.

[54] G. Mohamed and B. Bacroix, "Role of Stored Energy in Static Recrystallization of Cold Rolled Copper Single and Multicrystals," vol. 48, no. 13, pp. 3295–3302, 2000.

[55] P. Longere, A. G. Geffroy, B. Leble, and A. Dragon, "Modeling the Transition between Dense Metal and Damaged (Microporous) Metal Viscoplasticity," *Int. J. Damage Mech.*, vol. 21, no. 7, pp. 1020–1063, 2012.

[56] S. H. Goods and L. M. Brown, "The Nucleation of Cavities by Plastic Deformation," *Acta Metall.*, vol. 27, no. 1, pp. 1–15, 1979.

[57] J. W. Hancock and A. C. Mackenzie, "On the Mechanisms of Ductile Failure in High-Strength Steels Subjected to Multi-Axial Stress-States," *j. Mech. Phys. Solids*, vol. 24, pp. 147–169, 1976.

[58] J. F. Kalthoff and S. Winkler, "Failure mode transition at high rates of shear loading.," in *Impact Loading and Dynamic Behaviour of Materials*, Vol. 1., C. Y. Chiem, H.-D. Kunze, and L. W. Meyer, Eds. 1987, pp. 185–195.

[59] M. Zhou, A. J. Rosakis, and G. Ravichandran, "Dynamically propagating shear bands in impact-loaded prenotched plates-I. Experimental investigations of temperature signatures and propagation speed.," vol. 44, no. 6, pp. 981–1006, 1996.

[60] P. P. W. Dornowski, "Localisation phenomena in thermo-viscoplastic flow processes under cyclic dynamic loadings," *Comput. Assist. Mech. Eng. Sci.*, vol. 7, pp. 117–160, 2000.

[61] M. Kulkarni, T. Belytschko, and A. Bayliss, "Stability and error analysis for time integrators applied to strain-softening materials," *Comput. Methods Appl. Mech. Eng.*, vol. 124, no. 4, pp. 335–363, 1995.

[62] R. Courant, K. Friedrichs, and H. Lewy, "On the Partial Difference Equations of Mathematical Physics," *IBM J. Res. Dev.*, vol. 11, no. 2, pp. 215–234, 1967.

[63] A. Needleman, "Material rate dependence and mesh sensitivity in localization problems," *Comput. Methods Appl. Mech. Eng.*, vol. 67, no. 1, pp. 69–85, 1988.

[64] W. M. Wang, L. J. Sluys, and R. De Borst, "Interaction between material length scale and imperfection size for localisation phenomena in viscoplastic media," *Eur. J. Mech. - A/Solids*, vol. 15, no. 3, pp. 447–464, 1996.

[65] Y. Bao and T. Wierzbicki, "On fracture locus in the equivalent strain and stress triaxiality space," *Int. J. Mech. Sci.*, vol. 46, no. 1, pp. 81–98, 2004.

[66] J. Wolf, P. Longère, J. M. Cadou, and J. P. Crété, "Numerical modeling of strain localization in engineering ductile materials combining cohesive models and X-FEM," *Int. J. Mech. Mater. Des.*, vol. 14, no. 2, pp. 177–193, 2018.

[67] T. Belytschko, S. Loehnert, and J.-H. Song, "Multiscale aggregating discontinuities: A method for for circumventing loss of material stability," *Int. J. Numer. Methods Eng.*, vol. 73, no. 1, pp. 869–894, 2008.

[68] H. Talebi, M. Silani, S. P. A. Bordas, P. Kerfriden, and T. Rabczuk, "A computational library for multiscale modeling of material failure," *Comput. Mech.*, vol. 53, no. 5, pp. 1047–1071, 2014.

[69] J. H. Song and Y. C. Yoon, "Multiscale failure analysis with coarse-grained micro cracks and damage," *Theor. Appl. Fract. Mech.*, vol. 72, no. 1, pp. 100–109, 2014.

[70] N. Jacques, S. Mercier, and A. Molinari, "Effects of microscale inertia on dynamic ductile crack growth," *J. Mech. Phys. Solids*, vol. 60, no. 4, pp. 665–690, 2012.

[71] H. Couque, "A Hydrodynamic Hat Specimen to Investigate Pressure and Strain Rate Dependence on Adiabatic Shear Band Formation," *J. Phys. IV. Fr.*, vol. 110, pp. 423–428, 2003.